

Methods to Measure and Relate the Viscoelastic Properties of Brain Tissue

by

Aleksandar S. Mijailovic

Submitted to the Department of Mechanical Engineering
in partial fulfillment of the requirements for the degree of

Master of Science in Mechanical Engineering

at the

MASSACHUSETTS INSTITUTE OF TECHNOLOGY

September 2016

© Massachusetts Institute of Technology 2016. All rights reserved.

Author: _____

AM
Signature redacted

Department of Mechanical Engineering
August 19, 2016

Certified: _____

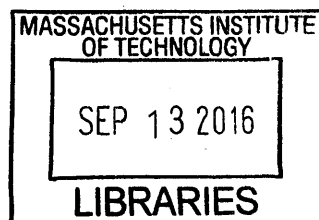
KJV
Signature redacted

Krystyn J. Van Vliet
Professor of Material Science and Engineering and Biological Engineering
Thesis Supervisor

Accepted by: _____

Signature redacted

Rohan Abeyaratne
Chairman, Departmental Committee on Graduate Students



ARCHIVES

Methods to Measure and Relate the Viscoelastic Properties of Brain Tissue

by

Aleksandar S. Mijailovic

Submitted to the Department of Mechanical Engineering
on August 19, 2016 in Partial Fulfillment of the Requirements
for the Degree of Master of Science in Mechanical Engineering

Abstract

Measurement of brain tissue elastic and viscoelastic properties is of interest for modeling traumatic brain injury, understanding and creating new biomarkers for brain diseases, improving neurosurgery procedures and development of tissue surrogate materials for evaluating protective strategies (e.g., helmets). However, accurate measurement of mechanical properties of brain tissue is challenging due to the high compliance and complex mechanical behavior of this tissue, including nonlinear viscoelastic behavior, poroelastic deformation, and failure mechanisms. Thus, reported measurements of the elastic and viscoelastic moduli of brain tissue vary by several orders of magnitude.

This thesis highlights three mechanical characterization techniques for brain tissue: rheology, cavitation rheology, and impact indentation. Rheology is used to measure the shear storage and loss moduli of brain tissue in (1) healthy and tuberous sclerosis mouse brain and (2) healthy porcine brain. Next, cavitation rheology – a technique used to measure the elastic modulus of compliant polymers and tissues – is implemented for the first time in porcine brain tissue. Finally, a new analytical model and analysis procedure are developed for impact indentation, a novel mechanical characterization technique that was used to measure the impact response of murine and porcine brain tissue and brain tissue simulant polymers. This new analytical model allows for measurement of viscoelastic moduli via impact indentation experimental data, and it directly relates viscoelastic moduli to impact indentation output parameters of quality factor, energy dissipation capacity, and maximum penetration depth without the need for finite element simulation.

Thesis Supervisor: Krystyn J. Van Vliet

Title: Professor of Material Science and Engineering and Biological Engineering

Acknowledgements

First and foremost, thank you to Krystyn for mentoring, teaching, and supporting me through this research process. Without you, this work would not have been possible. Thank you to Bo, Frank, Liz, and Aurelie for working with me on this project, and to the rest of the Van Vliet group and ISN team for your guidance, support and patience over the last two years. Thank you mom, dad, Ana, Vida, Aleks, Ellie, Julian, Zotti, Andrew, Dan, Dan, Greg, David, Leslie, and Chris for all the love, encouragement, and help through this process. Thank you to Professor Kamm, Professor Grodzinsky, Professor Mikić, Professor Townsend and Professor Karnik for your excellent teaching and mentoring in my coursework and research.

Table of Contents

Abstract.....	3
1 Introduction	7
1.1 Motivation.....	7
1.1.1 Disease may alter mechanical properties of brain tissue	7
1.1.2 Modeling brain injury	8
1.1.3 Creating tissue simulant materials for protective strategies	11
1.2 Methods for measuring and modeling the mechanical behavior of brain tissue.....	13
1.2.1 Viscoelastic models	13
1.2.2 Hyperelastic models.....	16
1.2.3 Nonlinear viscoelastic models	18
1.2.4 Measuring the mechanical properties of brain tissue.....	18
1.2.5 Origin of mechanical properties: Microstructure of the tissue	21
1.3 Thesis organization	22
2 Macroscale rheology of mammalian brain tissue.....	23
2.1 Introduction.....	23
2.2 Brain mechanical properties in a tuberous sclerosis mouse model.....	24
2.2.1 Background.....	24
2.2.2 Methods.....	25
2.2.3 Results.....	26
2.2.4 Discussion.....	26
2.3 Rheology of healthy porcine brain tissue.....	29
2.3.1 Background.....	29
2.3.2 Methods.....	29
2.3.3 Results.....	30
2.3.4 Discussion.....	30
3 Cavitation rheology of mammalian brain tissue.....	32
3.1 Introduction.....	32
3.2 Background	32
3.3 Methods.....	34
3.3.1 Brain samples.....	34

3.3.2	Cavitation rheology procedure.....	35
3.4	Results.....	36
3.5	Discussion.....	37
4	Impact indentation of compliant viscoelastic materials: A new analytical framework and connection to other experimental techniques.....	40
4.1	Introduction.....	40
4.2	Background.....	41
4.2.1	Simple mass spring dashpot system.....	41
4.2.2	Impact indentation experimental method.....	42
4.2.3	Original analysis of impact indentation data.....	44
4.2.4	Previous finite element modeling.....	45
4.3	Limitations of the previous model & data analysis: Effect of load on K and Q	46
4.4	A new analytic model of impact indentation.....	52
4.4.1	The relationship between K and Q	52
4.4.2	Quantifying x_{max}	54
4.4.3	A differential equation for impact on a viscoelastic material.....	55
4.4.4	Solutions to “pure impact”: New analytic methods for Q	58
4.4.5	A technique for measuring viscoelastic moduli by impact indentation.....	60
4.4.6	Methods for determining the poles from experimental impact indentation response: Logarithmic decrement and systems identification.....	61
4.4.7	Measuring material properties from impact indentation data: Proof of concept....	62
4.4.8	Effect of geometry and mass of the impacter on the outcome variables.....	66
4.4.9	A complete mathematical model for impact indentation experiments.....	66
4.5	Discussion.....	68
5	References.....	71
6	Appendix.....	76

1 Introduction

1.1 Motivation

Measurement of the elastic and viscoelastic properties of brain tissue are of interest for understanding disease and neural development, modeling traumatic brain injury, modeling neurosurgery, and creating tissue simulant materials. In this thesis, we use and develop three experimental techniques – rheology, cavitation rheology, and impact indentation – that can be employed to obtain key mechanical properties of interest for mechanically compliant, hydrated tissues such as brain tissue.

1.1.1 Disease may alter mechanical properties of brain tissue

Disease often affects the composition and structure of biological tissues. These changes may affect mechanical properties of such tissues, such as stiffness. Understanding and measuring these changes may be useful in biotechnology and in medicine, as the mechanical properties may be correlative with disease pathology¹⁻⁵ or for design of materials that mechanically mimic tissue at specific stages of disease or injury.⁶ For example, for diseases that do not currently have useful biomarkers, mechanical properties such as stiffness may be used as a marker of disease progression, correlative with structural alterations (e.g., destruction of axon networks or myelinated regions of the central nervous system) that are characteristic of the disease.¹

Alteration in the elastic and viscoelastic properties of brain tissue has been observed in various brain diseases including in Alzheimer's disease,² multiple sclerosis,⁵ glioma,³ in demyelinated brain⁴ and even in normal aging.^{7,8} Disease models have been studied by various methods, and in various models both *in vivo* and *ex vivo*.^{3,4} For example, *in vivo* magnetic resonance elastography experiments showed that stiffness of the brain was decreased in Alzheimer's patients comparing to controls (asymptomatic patients).² Stiffness of glioma tumors

in brain tissue was measured in mouse models via rheology and indentation, and found to be stiffer than healthy brain tissue.³ While *in vivo* measurement of properties is generally preferred to *ex vivo* due to clinical relevance,¹ only magnetic resonance elastography – a very expensive method – can currently measure *in vivo* brain mechanical properties.⁹ Often, disease models in rodents are preferred, as they are easily implemented and rodents are more easily maintained than larger animals (e.g., pigs).

1.1.2 Modeling brain injury

There are over 10 million cases of traumatic brain injury (TBI) annually,¹⁰ with approximately 1.7 million cases and about 50,000 deaths in the United States alone.¹¹ While 75% of these cases may be considered minor or concussive, sufferers of TBI may have devastating and permanent effects, such as depression, cognitive deficits, and aggressive behaviors.¹² Some causes may not be preventable with protective equipment (e.g., falls, assaults), but TBI due to automobile accidents, contact sports and military combat – cases that may be highest risk for mortality and permanent disability – could be mitigated with better helmets, airbags or safety features.

Modeling of impacts to the head may be investigated for design of protective strategies and to understand how the brain is injured. Most modeling has been carried out by finite element methods^{13,14} for a variety of loading conditions, including impact loading,^{13,15} blast wave,¹³ pressure, and neurosurgery (**Figure 1.1**).¹⁶ The nature of these simulations heavily depends on regimes of loading conditions. For example, for low speed impact, viscoelastic effects will be dominant. However, if the impact speed is high, the material will not have time to relax and dissipate energy (depends on time constants) and glassy modulus will be more relevant. Depending on the magnitude of the load, failure parameters such as critical stress or strain

thresholds,¹³ may be relevant in both conditions. Moreover, if deformations are large such that material response is nonlinear elastic or nonlinear viscoelastic, then nonlinear material models should be included.¹⁷

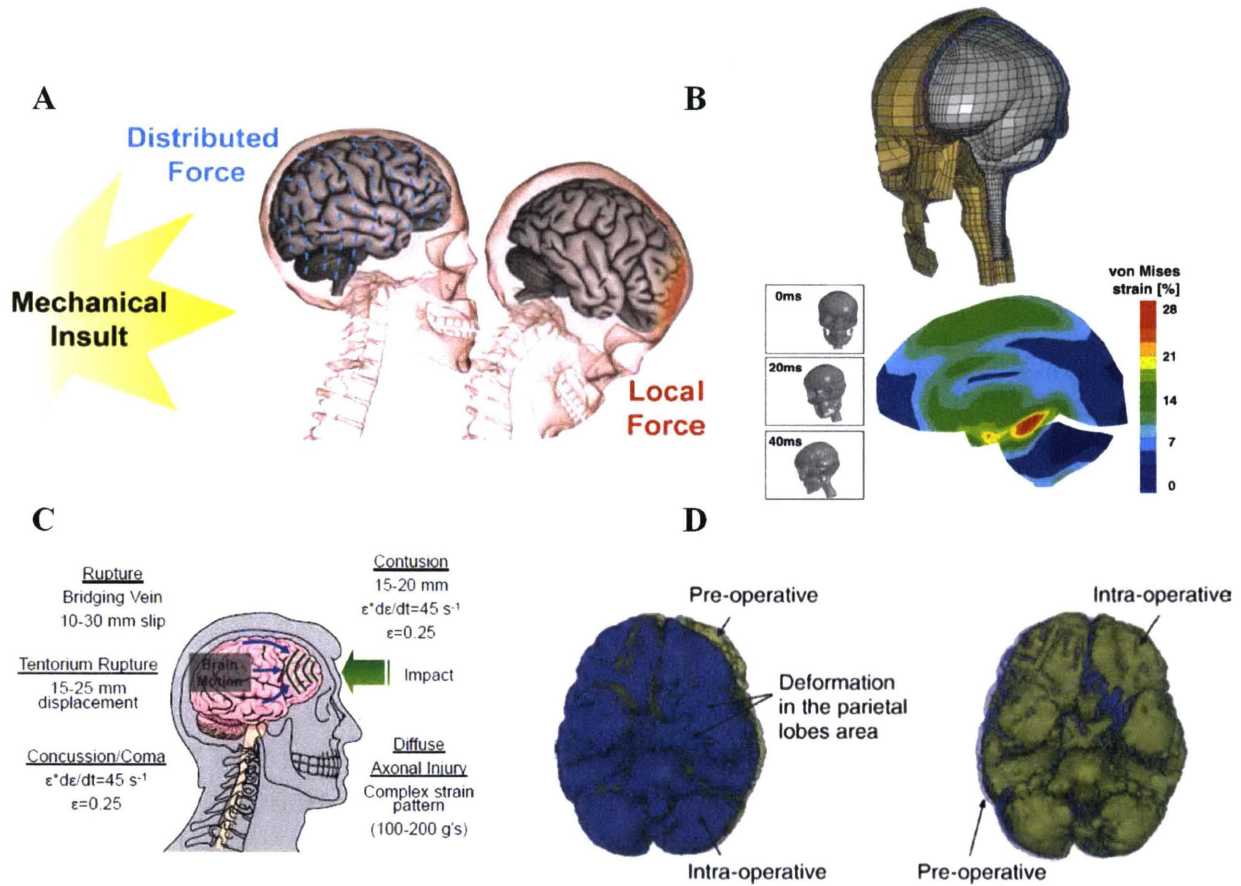


Figure 1.1: Modeling brain injury. (A) TBI can be caused by many different loading mechanisms, which may result in distributed or localized forces. (Adapted from Hemphill et al.)¹⁸ (B) A finite element model of a sports injury impact. (Adapted from Cloots et al.)¹⁹ (C) When interpreting simulated results, strain and strain rate thresholds may be used as indicators for TBI events. (From the review of Department of Defense Test Protocols for Combat Helmets).²⁰ (D) A finite element model used to evaluate neurosurgery procedures. (Adapted from Miller et al.)²¹

When modeling traumatic brain injury, common outcome parameters include pressure, von Mises stress and strain and maximum principal strain. These results can be assessed to determine if the deformations or stresses reach failure, thus indicating brain damage via axonal shearing.¹³ However, the spatially inhomogeneous structure on the microstructural level of the

brain makes accurate failure criteria difficult.¹⁸ For example, it has been suggested that the microvasculature in the brain may amplify stresses and strains in surrounding axons, which in turn produces axonal damage in those areas.^{18,19} Additionally, anisotropic effects can considerably alter stress and strains locally in the brain, and thus regions like the corpus collosum maybe more susceptible to injury than others.¹⁵ Therefore, while extremely useful for engineering purposes, models using homogenous, bulk mechanical properties of the brain may not be able to accurately model injury. Critical volume elements may be used for efficient multiscale modeling.¹⁵

Constitutive laws used for modeling include viscoelasticity, hyperelasticity, and more advanced models such as hyper-viscoelasticity;^{13,17,19} these models are described in depth in the following section. For modeling of human traumatic brain injury, porcine or bovine brain measurements have been used to determine material properties, as they are structurally similar in terms of quantity of white and gray matter (**Figure 1.2**).^{17,22}

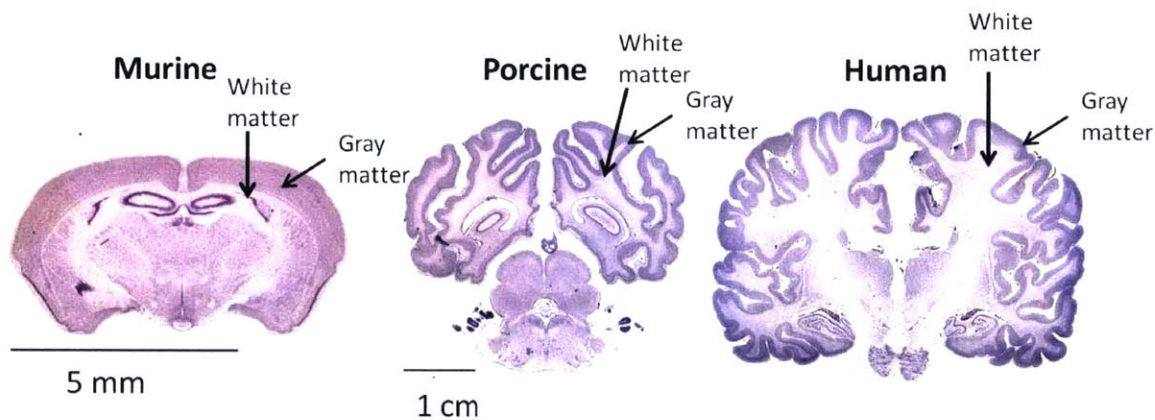


Figure 1.2: Coronal brain histological slices from murine, porcine and human brain. Larger animals tend to have increased cortical folding and a higher proportion of white matter. Structurally, it is clear that for simulating human brain mechanics, porcine is a better structural model than murine brain. (Figure from <http://brainmuseum.org>)

1.1.3 Creating tissue simulant materials for protective strategies

Creating protective equipment preventing TBI is of high interest to national defense, the automobile industry, the contact sports industry and public health. To evaluate the efficacy of new protective equipment, tissue simulant materials that accurately mimic the mechanical response of brain tissue under specific loading conditions must be used (**Figure 1.3**); however, some materials that are currently used may be unrealistic. For example, standard protocol for helmet testing in the United States Army Research Laboratory, uses Roma Pastelina #1 ballistic clay.²⁰ This ballistic clay (as well as ballistic gelatin²³) is more than an order of magnitude stiffer than brain tissue.²⁴ We note that brain tissue under static/quasistatic loading and linearly elastic regime has a Young's modulus from hundreds of Pa to a few kPa, depending on the mechanical characterization technique.^{25,26,3} Creating a good match is challenging, as the elastic and damping properties of tissues may be a function of applied strain, strain rate, and the direction of the deformation if the tissue is anisotropic;³ further, the failure properties may be difficult to replicate.

Recent work from Van Vliet et al. and the U.S. Army Research Laboratory has focused on making polymers with tunable viscoelastic moduli in an effort to make more realistic tissue simulant materials.^{6,27} Compliant, viscoelastic polydimethylsiloxane (PDMS) polymers have been optimized to successfully match impact response of heart tissue (**Figure 1.3C**).⁶ More recently, multilayer gel composites with a compliant top layer have matched the impact response (via instrumented impact indentation) of more compliant brain tissue (**Figure 1.3D**).²⁸ However, more research is necessary to improve tunability in different loading conditions and to understand how to appropriately use these materials in testing of protective equipment. For example, the clay used in ballistics research currently is useful because it records energy

dissipation through plastic deformation.²⁰ Methods to measure the viscoelastic (and failure) responses would have to be developed prior to useful implementation of these materials for evaluation of protective strategies.

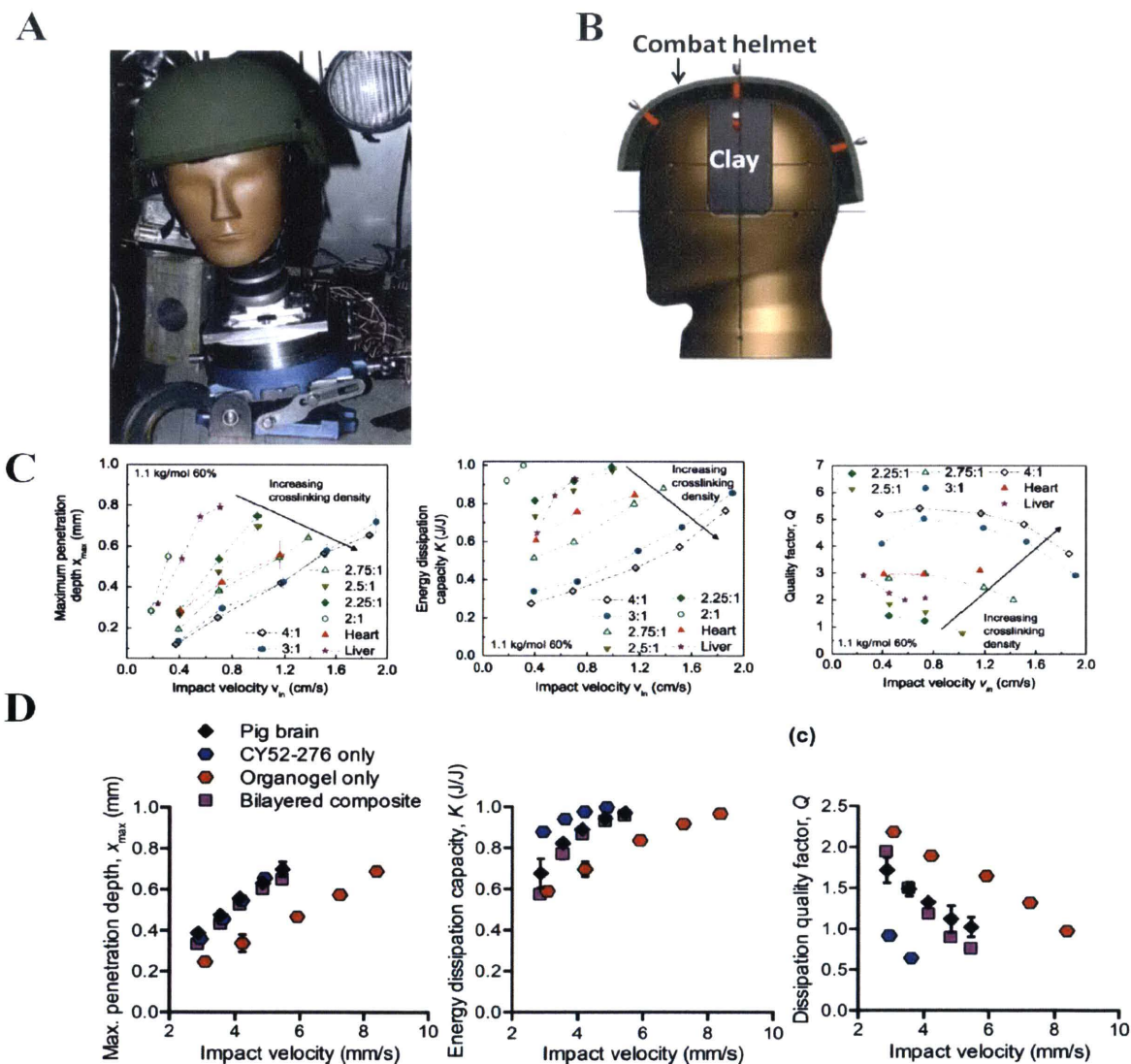


Figure 1.3: Tissue simulant materials for testing protective equipment. (A) Head model used for measurements. (B) Manikins are filled with a tissue surrogate substance, like ballistic gelatin or clay. ((A) and (B) adapted from the review of Department of Defense Test Protocols for Combat Helmets.)²⁰ (C) Impact indentation results for PDMS-based tissue simulant materials and murine heart and brain tissue. Impact velocity vs. maximum penetration depth, energy dissipation capacity, and quality factor is shown as a function of impact velocity. Recent work from Van Vliet et al. has successfully tuned the impact response of simulant polymers to that of heart but not of more compliant liver. (Figure adapted from Kalcioğlu et al.)⁶ (D) The impact indentation response of brain has been replicated using a bilayer composite gel. (Figure adapted from Qing et al.)²⁸

1.2 Methods for measuring and modeling the mechanical behavior of brain tissue

Many methods have been used for measuring mechanical properties of compliant polymers and soft tissues, such as brain tissue, and depend on the material properties of interest. Elastic and viscoelastic properties are of great interest in the literature, and the tissue is often assumed to be linear, isotropic and incompressible. Nevertheless, other properties such as poroelasticity, nonlinearity (e.g., hyperelasticity), and failure have been investigated. Further complicating analysis, brain tissue is anisotropic, nonhomogeneous, nonlinear, and properties may vary by length scale.^{9,29,30} Attempts at developing constitutive laws have been made recently.^{22,31–33} However, there is currently no consensus on a constitutive law in the literature,^{9,34} and measurements by different groups vary by as much as three orders of magnitude.^{9,30} We begin with two common models that are used in this thesis: viscoelastic and hyperelastic material models. Next we will review existing methods used to measure mechanical properties of brain tissue, and finally we will consider the structural origin of these mechanical properties.

1.2.1 Viscoelastic models

Mechanical models of biological tissues have generally borrowed from polymer mechanics. The structure of soft tissues is generally similar to crosslinked hydrated polymers, albeit more complicated (see **Section 1.2.5**). For small deformations, viscoelastic models describe the mechanical response of tissue reasonably well.^{35,36}

The general constitutive law in linear viscoelastic materials may be expressed as a function of time by the Boltzmann superposition principle:

$$\sigma_{ij} = \int_0^t S_{ijkl}(t-t') \frac{\partial \epsilon_{kl}}{\partial t'} dt' \quad (1.1)$$

$$\text{or } \epsilon_{ij} = \int_0^t C_{ijkl}(t-t') \frac{\partial \sigma_{kl}}{\partial t'} dt'$$

where σ_{ij} is the stress tensor, ϵ_{kl} is the strain tensor, S_{ijkl} is the stiffness tensor and C_{ijkl} is the compliance tensor. Similarly to linear elasticity, for isotropic materials the stiffness tensor S_{ijkl} may be represented in terms of two independent components, such as Young's modulus and Poisson's ratio, shear and bulk modulus, or Lamé constants; however, in viscoelasticity, these components are functions of time. Generally, the viscoelastic moduli of tissue are measured experimentally via frequency dependent storage and loss moduli (e.g., G' , E' , and G'' , E''), relaxation functions (e.g., $E(t)$, $G(t)$), or the related creep compliance function ($J(t)$). While these properties are measured in different ways, they can be related mathematically using Fourier or Laplace transforms. In our analysis, it will be convenient to represent the modulus as a shear relaxation function $G(t)$, and either bulk relaxation function $K(t)$ or Poisson's ratio $\nu(t)$.

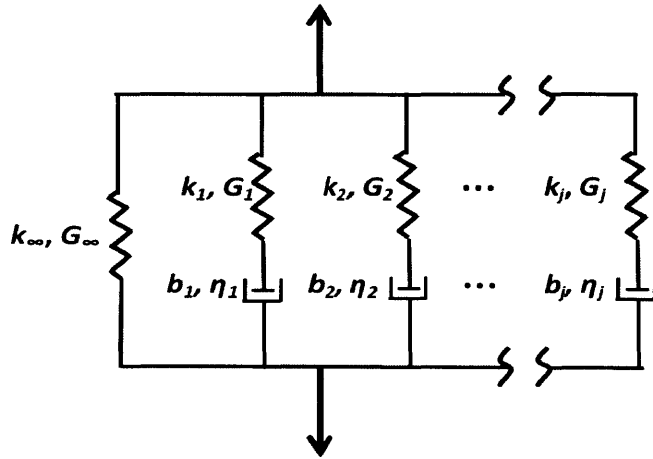


Figure 1.4: The generalized Maxwell model. A generalized Maxwell model is composed of a spring in parallel with N Maxwell elements (springs and dashpots in series). Each spring has a stiffness k , which can be converted to a shear modulus G , and each dashpot has a damping coefficient b which can be converted to a viscosity η . The time constant associated with each Maxwell element is $\tau=b/k= \eta /G$.

The most common model used to describe the shear relaxation is the generalized Maxwell model. This model is composed of one spring in parallel with N springs and dashpots in series (**Figure 1.4**). The stiffness of the springs may be expressed in terms of stiffness k or shear modulus G , and the dashpots may be expressed as the damping constant b or viscosity η . The physical interpretation is that the model has a distribution of N relaxation times. Upon instantaneous loading, all springs in parallel are deformed, and a stiff “instantaneous” or “glassy” shear elastic modulus G_0 governs the time response; however, at infinite time, the components with dashpots will all relax, and only the single spring will elicit an elastic response, and a more compliant shear “relaxation” modulus G_∞ . The governing differential equation for this model (in one dimension) may be expressed in the frequency domain as:

$$\bar{\sigma} = \left(G_\infty + \sum_{j=1}^N \frac{G_j s}{s + 1/\tau_j} \right) \bar{\epsilon} \quad (1.2)$$

Where $\bar{\sigma}$ and $\bar{\epsilon}$ are the Laplace transform of the (shear) stress and strain, respectively, G are (shear) moduli of the springs, $\tau_j = \eta_j / G_j$ where η is a dashpot constant, and s is frequency. The kernel for the equation is the relaxation function or the Prony series, and can be expressed in the time domain as:

$$G(t) = G_\infty + \sum_{j=1}^N G_j e^{-\frac{t}{\tau_j}} \quad (1.3)$$

or

$$G(t) = G_0 - \sum_{j=1}^N G_j (1 - e^{-\frac{t}{\tau_j}})$$

In the frequency domain, this can be expressed in terms of real and imaginary parts (or equivalently complex modulus and phase lag):

$$G'(s) = G_\infty + \sum_{j=1}^N \frac{G_j s^2 \tau_j^2}{1 + s^2 \tau_j^2} \quad (1.4)$$

$$G''(s) = \sum_{j=1}^N \frac{G_j s \tau_j}{1 + s^2 \tau_j^2} \quad (1.5)$$

These expressions are mathematically equivalent, and may be used in either form to fit data. Rheology and dynamic mechanical analysis (DMA), for example, are more easily fit in the frequency domain, while relaxation (or creep compliance) may be fit in the time domain. In **Chapter 4**, we will relate rheology parameters to impact indentation experimental data using these mathematical relationships. We note that while in viscoelastic theory the bulk modulus $K(t)$ may also relax, it is also assumed that tissues and polymers are incompressible ($\nu = 0.5$) and thus $K = \infty$. This allows facile conversion of shear modulus to Young's modulus:³⁶

$$\bar{E}(s) = 2(1 + \nu)\bar{G}(s) \quad (1.6)$$

The mechanical behavior of tissues often leads to power laws in the frequency domain instead of discrete time constants. Physically this corresponds to an infinite distribution of time constants, which cannot be fit perfectly with a discrete number of time constants. However if enough parameters are used, a usable fit may be obtained. A more complete power law behavior has been encapsulated using fractional derivative models using a single parameter³⁷ but is not commonly used. Assumptions of the viscoelastic model that we use in this work are that the material is (1) isotropic, (2) homogenous, (3) incompressible (4) linearly viscoelastic, (5) and only relaxes in shear (i.e., bulk modulus is constant).

1.2.2 Hyperelastic models

Another common constitutive model used in tissue mechanics is hyperelasticity. Hyperelastic theory also comes from the theory of polymers, and is useful for modeling large

deformations (sometimes nonlinear deformations) that may lead to nonlinear elastic properties. These constitutive laws often fit the strain stiffening behavior of tissues well; however, hyperelasticity assumes perfectly elastic deformation, which is problematic for modeling viscoelastic behavior.³⁵

The constitutive law in hyperelastic models is defined by a strain energy density function W , which is a function of strain e_{ij} :

$$\sigma_{ij} = \frac{\partial W}{\partial e_{ij}} \quad (1.7)$$

Since nonlinear deformations are often of interest, deformation is often defined in terms of stretch ratio, deformation gradient, or invariants of the stress tensor instead of engineering strain. The derivative of this strain energy density function with any deformation measurement results in stress (e.g., Cauchy stress, 1st Piola-Kirchoff stress, etc.)³⁵

The simplest hyperelastic model is the neoHookean strain energy function, which may be derived from entropic elasticity of polymer chains (which is the origin of elasticity in some but certainly not all polymers).³⁵ For isotropic, incompressible materials, the neoHookean strain energy function may be expressed in terms of the principal stretches $\lambda_1, \lambda_2, \lambda_3$ and shear modulus G as:

$$W = \frac{1}{2}G(\lambda_1^2 + \lambda_2^2 + \lambda_3^2 - 3) \quad (1.8)$$

We note the convenience that this nonlinear constitutive law can be described in terms of only the shear modulus G . The neoHookean model is the basis of the analysis of the cavitation rheology mechanical characterization technique, which is discussed in **Chapter 3**.

More sophisticated hyperelastic strain energy density functions such as the Mooney-Rivlin, Arruda-Boyce, or Fung modes, which have both empirical and first principal origins, often produce better curve fits to experimental data.^{35,38} However, these models also involve fitting more parameters, which are difficult to translate to moduli, such as a Young's and shear modulus. These models will not be addressed in this thesis.

1.2.3 Nonlinear viscoelastic models

Unfortunately, viscoelastic and hyperelastic models are often insufficient to accurately model polymers' and tissues' mechanical behaviors. Various nonlinear viscoelastic models, which combine principals of hyperelasticity and viscoelasticity, have been developed, including quasilinear viscoelastic models, and more complicated constitutive laws have been used in finite element modeling of brain tissue.^{19,22,35} These models will not be addressed in this thesis.

1.2.4 Measuring the mechanical properties of brain tissue

Measurements of the Young's elastic modulus E of brain range from 100s of Pa to 10s of kPa in the literature.^{9,30,39} However, since brain tissue behaves viscoelastically, the measurement of E is highly dependent on experimental loading conditions (such that its magnitude may approach either a glassy or relaxation modulus).

Brain mechanical properties have been measured *ex vivo* and *in vivo* on different length scales. Elastic and viscoelastic properties of *ex vivo* brain on the tissue level have been measured by unconfined uniaxial compression or tension,^{40,41} relaxation in shear^{7,42} and compression,^{7,22} instrumented indentation,²⁶ and shear rheology.^{3,9,17,42,43} Magnetic resonance elastography has been used to measure *in vivo* storage and loss moduli in mice⁴ and humans.^{1,2,44} On the

microscale level, atomic force microscope (AFM)-enabled indentation has been used.⁴⁵ On the cellular level, viscoelastic properties have been measured by AFM and optical stretching.⁴⁶

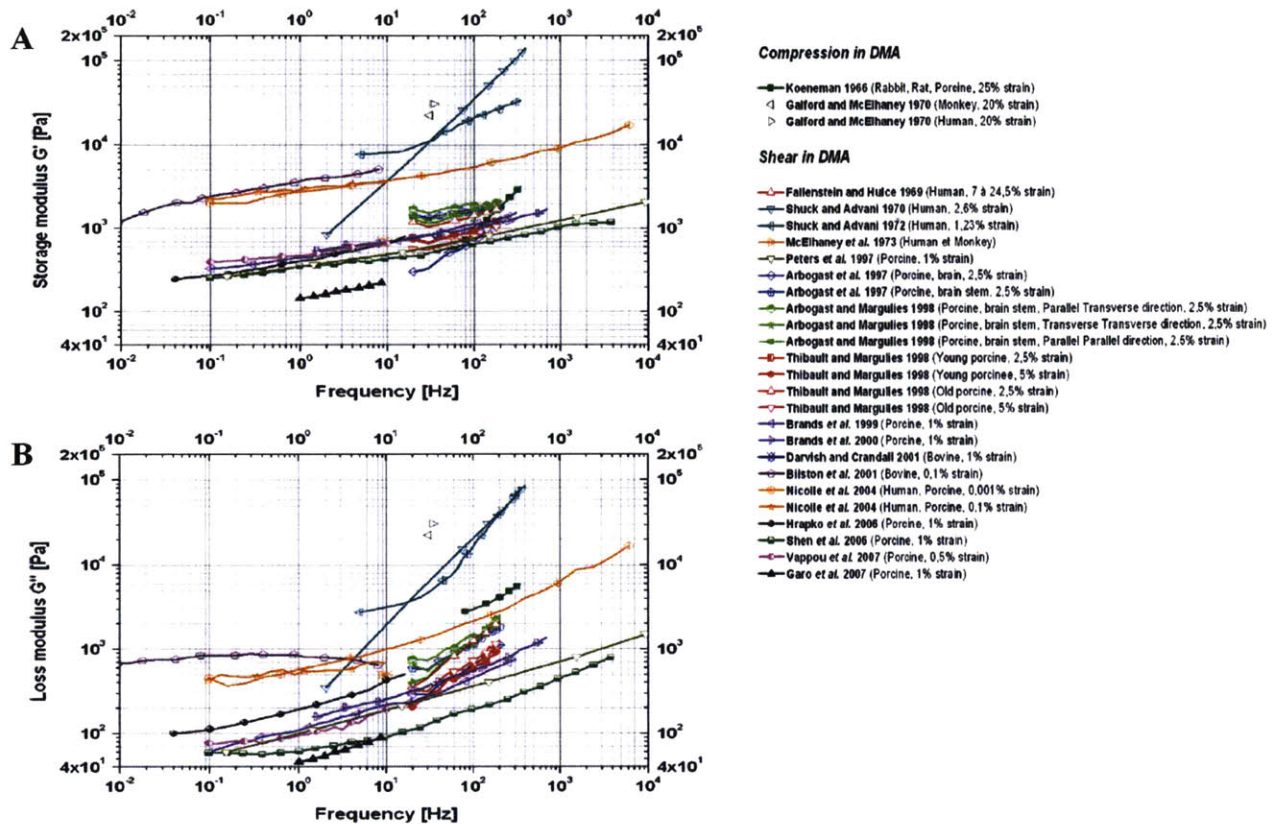


Figure 1.5: Shear rheology in the literature. (A) G' and (B) G'' shear rheology and compressive DMA measurements for porcine, bovine, rat, rabbit, and human brain tissue from various studies. There is considerable variability between measurements; however G' tends to be on the order of 10^3 - 10^4 Pa, whereas G'' is on the order of 10^2 - 10^3 . Additionally, while both G' and G'' exhibit weak power laws with nearly identical slopes in most studies, G'' appears to be considerably steeper, and thus $\tan\delta$ increases with frequency. Figure adapted from Chatelin et al.⁹

On the length scale of the tissue, shear rheology measurements for G' and G'' by different groups also span orders of magnitude, but as shown in the review by Chatelin,⁹ there is consistency in a subset of studies, with G' being on the order of 100s to 1000s of Pa, and G'' on the order of 10s to 100s of Pa, depending on frequency (**Figure 1.5**). In almost all cases, G' and G'' are characterized by weak power laws, meaning that the exponent defining the power is the slope of the line in a log-log plot of modulus vs. frequency.^{9,21}

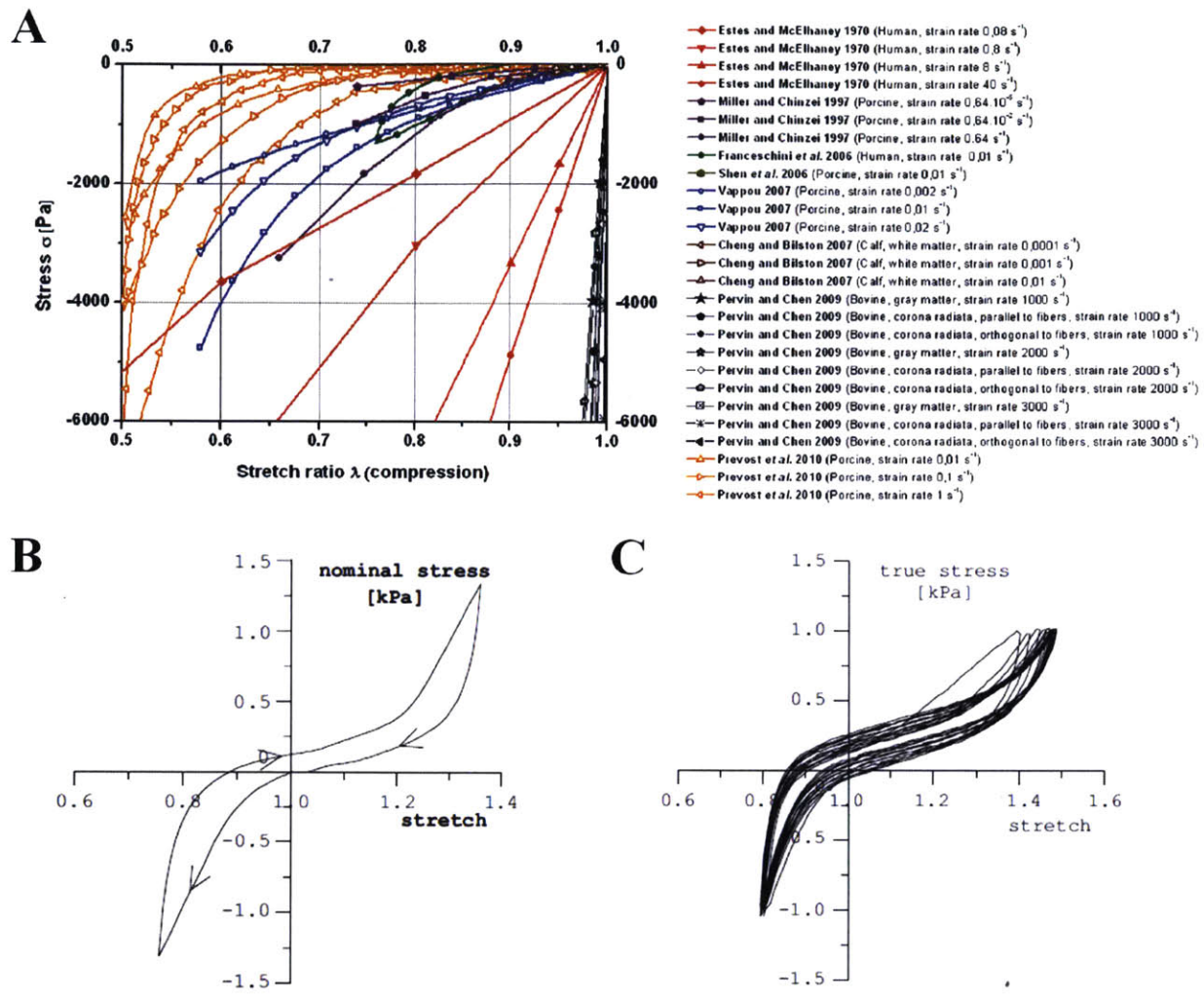


Figure 1.6: Nonlinear material behavior of brain in tension and compression. (A) High compressive deformation yields nonlinear behavior in a variety of species and brain regions. (Adapted from Chatelin et al.)⁹ (B) A tension-compression deformation cycle for brain shows nonlinear response. (C) Preconditioning is observed, as stiffness decreases for several deformation cycles, but is consistent afterward. (B) and (C) adapted from Franceschini et al.²⁹

While most studies have focused on moduli in the linear range, the brain exhibits strain stiffening under large strains, as has been shown by cyclic uniaxial tension/compression tests (Figure 1.6).²⁹ The brain also has heterogeneous mechanical properties on the macroscale, as studies have shown that white matter is stiffer than gray matter.^{1,7,26} There are also local

variations in white matter stiffness,^{1,7} with the corpus collosum white matter reported in some studies to be stiffer than the corona radiata and other white matter.¹ White matter has also been found to be mildly anisotropic due to the directionality of axon bundles,⁷ but with stiffnesses varying by up to a factor of two in different directions.^{21,26} Further, the brain, which is composed of 20% extracellular fluid,⁴⁷ has been shown to behave poroelastically at low strain rates.^{41,29} Like many other tissues,³⁵ the preconditioning phenomenon (i.e., changing of stiffness upon the first few loading cycles until material properties converge) has also been observed in brain tissue (**Figure 1.6C**).⁷

1.2.5 Origin of mechanical properties: Microstructure of the tissue

Brain tissue is characterized by a highly heterogenous hierarchical structure – from the tissue level, to the cellular level, to the molecular level. On the tissue level, properties arise from different tissue types: gray matter – composed of cell bodies – is isotropic and relatively compliant comparing to white matter. White matter is composed of stiffer axon bundles, which form anisotropy due to directionality of the axon connections.³⁰ Different regions of the brain contain different amounts of white and gray matter and fluid filled ventricles, and the geometry of the brain is complicated due to folding and other structures;²¹ brain structure and white and gray matter content vary considerably by species (**Figure 1.2**). Generally speaking, the extracellular matrix protein networks that cells produce and to which cells adhere form the structural and mechanical medium of the tissue.³⁰ (Interestingly, while the effective crosslinks within such protein networks behave like covalent ones in conventional polymers, most biological polymers are held together by van Der Waals forces between large monomers.)⁴⁸

On the length scale of the cell, there is further complexity. There are different types of cells that have different stiffness (e.g., astrocytes vs. neurons),⁴⁶ and different components of cells that

have different stiffnesses (soma vs. cell processes).^{30,46} The brain is also relatively porous, and is composed of approximately 20% extracellular space, and has therefore shown to have a poroelastic response.^{29,47} It is thought that most of the elastic response of the tissue is due to cellular components, as the extracellular matrix is largely composed of glycosaminoglycans such as hyaluronic acid, and has very few fibrous proteins (e.g., collagen), except for in the basement membrane.^{30,49} The intercellular space of neuron cell bodies and astrocytes is similar to that of many mammalian cells, with elasticity arising from actin, intermediate filaments and tubulin. The structure on the cellular level is clearly inhomogeneous as well.⁴⁶

1.3 Thesis organization

In this thesis, we will explore three methods for measuring the elastic and viscoelastic properties of brain tissue.

In **Chapter 2** we use shear rheology to measure the dynamic moduli of healthy and tuberous sclerosis mouse brain to investigate whether the disease affects the brain mechanical properties. We also measure the dynamic moduli of healthy porcine brain tissue which will be used to compare with cavitation rheology in **Chapter 3**.

In **Chapter 3** we present the first use of cavitation rheology to measure the Young's modulus of brain tissue, and validate the results via shear rheology.

In **Chapter 4** we develop a new theoretical model for impact indentation experiments. From the governing equations, we illustrate how to better design experiments, relate rheology and impact indentation data without finite element simulation, improve accuracy of analysis of impact indentation data, and extract viscoelastic moduli from impact indentation experiments.

2 Macroscale rheology of mammalian brain tissue

2.1 Introduction

Shear rheology is a powerful experimental technique used to mechanically characterize viscoelastic solid materials and complex fluids at the macroscale. In the field of tissue mechanics, the shear storage modulus G' and loss modulus G'' (or equivalently the complex modulus G^* and phase lag δ) are measured, and a parallel plate probe geometry is often used (**Figure 2.1**). In the technique, the sample is placed in between the two plates, and the top plate twists the sample an angle amplitude φ_0 at a frequency ω , resulting in a deformation with a strain amplitude of γ_0 . From the amplitude of the resulting torque signal T_0 phase lag Φ between the angular displacement and torque are measured. From these parameters, G' and G'' can be determined from geometric expressions. Measurements are taken at a variety of prescribed

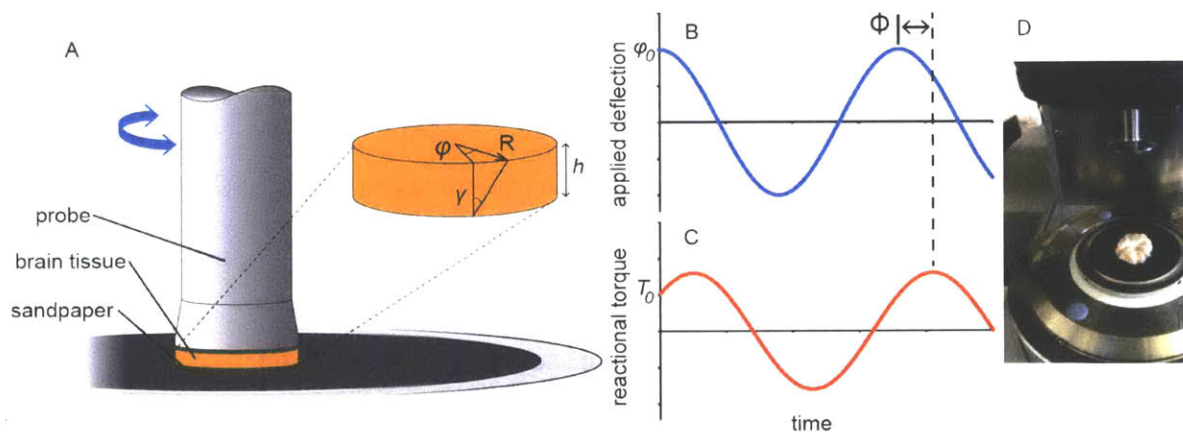


Figure 2.1: Rheology experimental setup. (A) The sample is placed between two rheometer plates, and sandpaper is attached to both plates to prevent slip. The top plate oscillates at a frequency ω and amplitude φ , resulting in a shear strain γ . Applied deflection (B) over time results in a reactional torque (C); G' and G'' may be measured from the phase lag Φ and amplitudes of the deflection φ_0 and torque T_0 . (D) A 25 mm diameter, 4 mm thick porcine brain slice on a rheometer plate prior to contact. (A)-(C) from Canovic et al.²⁵

frequencies, and generally range from 0.001 to 100 Hz, with limitations at the lower end being signal to noise ratio, and on the upper end inertial effects.⁵⁰

If the material is homogenous and elastically isotropic, torsion suggests that shear strain/shear stress is linear with increasing radius r . Thus, the amplitude of the nominal shear strain is actually the maximum shear strain at the sample, located at the edge of the probe, and the shear strain is zero at radius $r = 0$. This also means that the center of the material contributes least to the measurements, and the edges contribute the most. Care must be taken to section the sample such that it fits the probe geometry well. If the material is inhomogeneous like brain tissue, rheology will only give an average measurement of the storage and loss moduli, which is often sufficiently useful for engineering purposes. Additionally, the material may have nonlinear elastic properties at large strains. For this reason, amplitude sweeps (i.e., changing shear strain amplitude) may be conducted to determine to which deformation linearity is maintained, and frequency sweeps should be conducted at a shear strain that is in this linear range.⁵⁰

The experiments reported in this thesis use shear rheology to quantify G' and G'' for mouse and porcine brain tissue, respectively.

2.2 Brain mechanical properties in a tuberous sclerosis mouse model

2.2.1 Background

Tuberous sclerosis (TSC) is a genetic disease that causes various symptoms, including neurological problems, and has high comorbidity with autism.⁵¹ The disease is caused by mutations in the *Tsc1* and *Tsc2* genes, and knockout mouse models have been made for the disease.⁵² It has been shown that these knockout mice have hypomyelination,⁵² and similar findings have been seen in humans via diffusion tensor imaging.⁵³ Since brains with

hypomyelination have been shown to have altered mechanical properties,⁴ we hypothesize that the structural differences in TSC mouse brains may lead to altered mechanical properties in the brain. Knowledge of these differences may be used for monitoring disease progression or for therapeutic targets, if altered mechanical properties contribute directly to the pathology of the disease.

On a structural level, hypomyelination should affect white matter of the brain more than gray matter, as white matter is mainly composed of myelinated axons, whereas gray matter has more cell bodies and astrocytes.³⁰ Mouse brain, unlike human or other large mammals' brains, has very little white matter, accounting for only about 10% of the structure; much of the white matter is located in the corpus callosum of the brain (**Figure 1.2**). In our study, we therefore measured the viscoelastic properties of brain both on the whole brain level via shear rheology, as well as on the local level with impact indentation (~1mm scale) and AFM instrumented indentation (μm scale).⁵⁴ This chapter focuses on the rheology measurements, and the measurements on the microscale are compared in the discussion.

2.2.2 Methods

2.2.2.1 Sample preparation

Tuberous sclerosis mouse models were bred as described previously.⁵² After sacrifice, whole brains were extracted and sliced to 1mm thickness, and were stored in Hibernate-A media (ThermoFisher Scientific, Waltham, MA) on ice. Measurements were conducted within 48 hours of sacrifice. The *Guide for the Humane Use and Care of Laboratory Animals* was followed for all procedures. The study was approved by the Animal Care and Use Committee of Children's Hospital, Boston and the Harvard Medical Area Standing Committee on Animals.

2.2.2.2 Rheology procedure

The procedure for rheology was described in Canovic et al.⁵⁴ Briefly, a parallel plate rheometer was used to measure G' and G'' at 25°C. A 10 mm diameter probe was used with a 1 mm thick sample, and sandpaper was adhered to both plates (320 grit, McMaster Carr) to prevent slip between the tissue and the plates. To provide consistent measurements, the normal force on the tissue was maintained at 0.01 N after the tissue was allowed to relax for approximately 5 minutes. To maintain hydration of a tissue, approximately 500 μ l of Hibernate-A media was pipetted to the sides of the tissue after contact was maintained. An amplitude sweep from 0.01% to 10% shear strain was conducted at 1 rad/s and 10 rad/s, and the viscoelastic range of the tissue was determined to be ~1-3% strain. Frequency sweeps from 0.1 to 10 Hz were conducted at 1% strain.

2.2.3 Results

Storage and loss moduli as a function of frequency for TSC and control mouse brain are plotted in **Figure 2.2**. Clearly there is no difference between TSC and control. The magnitude and trend of these data are consistent with other studies of healthy porcine^{9,17} and murine³ brain tissue rheology.

2.2.4 Discussion

Rheology data suggest that there is no different in viscoelastic properties in TSC vs control mice. These data agree with other measurements by our group which show no difference between the two groups.⁵⁴ Creep compliance and stress relaxation experiments via AFM enabled indentation showed no significant difference between disease and control at 10 s of loading. Additionally impact indentation showed no significant difference between TSC and control for maximum impact depth, energy dissipation capacity, and quality factor for all impact speeds

investigated.

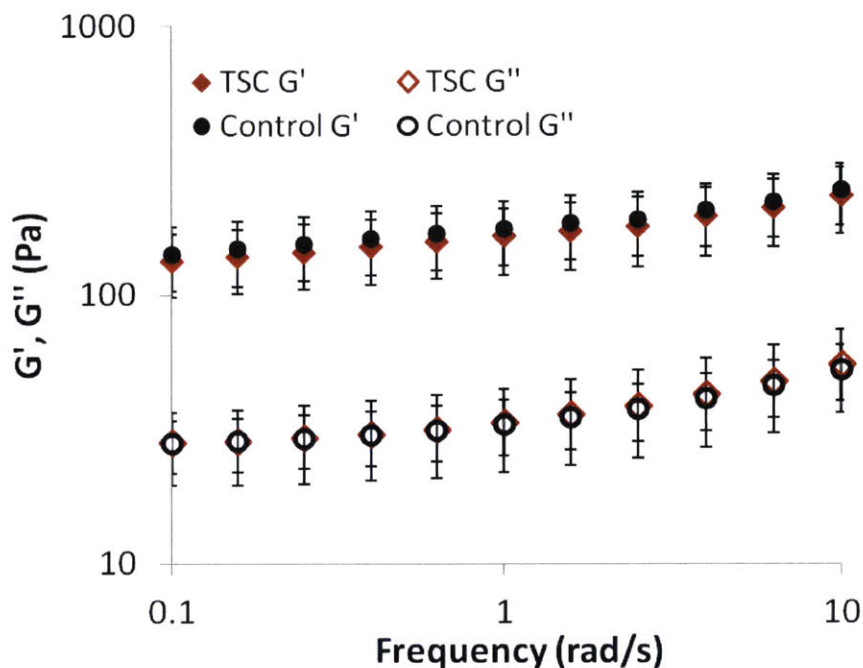


Figure 2.2: Rheology for TSC and wild-type brain tissue. Storage (G') and loss (G'') moduli of TSC (red) and wild-type brains (black). $n=5$ for TSC mice and $n=7$ for wild type mice. Error bars represent standard deviation.

These data suggest that the structural difference in TSC mouse brain (namely a decrease in myelin) do not elicit a difference in mechanical properties. The structural differences are concentrated in the white matter of the brain, which is mostly composed of myelinated axons. We note that the rheology probe is too large to measure gray and white matter individually, as the probe diameter is on the length scale of the whole mouse brain. However, AFM indentation experiments (**Figure 2.3**), which probe mechanical properties on the length scale of $\sim 10 \mu\text{m}$ also did not show differences between TSC and control in both white and gray matter for creep compliance and stress relaxation at 10 s, but showed that the modulus of gray matter is higher

than white matter. This contradicts previous studies that suggest that white matter is stiffer,^{7,26} and the reason for this discrepancy is unclear.

These results also contradict a recent study that showed that hypomyelination of mouse brain tissue resulted in a decrease in stiffness compared to control, measured via magnetic resonance elastography.⁴ However, the mechanism of demyelination in that study was induced chemically via cuprizone, which also caused alterations in the extracellular matrix and cellular composition.⁴ It is unclear if the hypomyelination played a role in the alterations of the brain's stiffness in that disease model.

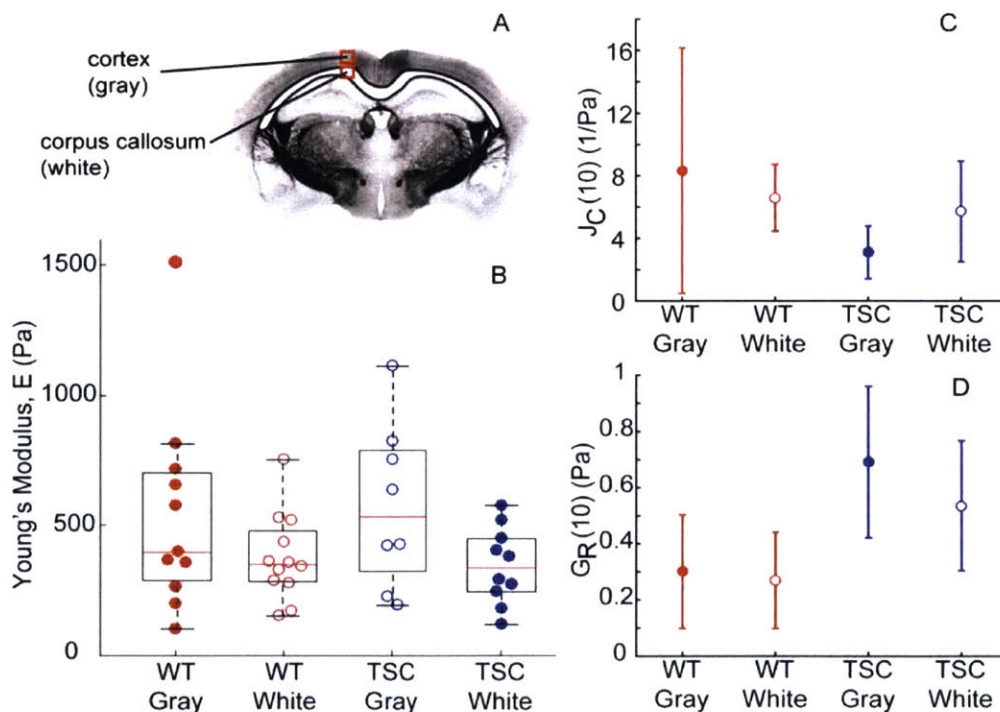


Figure 2.3: Indentation of TSC and wild type mouse brain. Indentation of TSC and wild type mouse brain shows no significant difference in elastic and viscoelastic properties. (A) Coronal view of the mouse brain. Gray matter was measured in the cortex, while white matter was measured in the corpus callosum. (B) Young's modulus, (C) creep compliance at 10 s and (D) stress relaxation at 10 s measurements showed no significant differences between TSC and wild type in both gray and white matter. Gray matter elastic modulus was significantly higher than white matter for both wild type and TSC groups (A), but no significant differences were seen between white and gray matter in creep compliance and stress relaxation measurements (C) and (D). Error bars represent standard deviation. Figure adapted from Canovic et al.⁵⁴

2.3 Rheology of healthy porcine brain tissue

2.3.1 Background

Since the porcine brain is structurally similar to human brain (**Figure 1.2**), material properties from porcine brain are commonly used to model traumatic brain injury. In this study, we use rheology to measure G' and G'' in porcine brain, and we investigate the effect of axial pre-strain on G' and G'' . We published the methods and data presented in this section in the Journal of Visualized Experiments.²⁵ In **Section 3.5** we compare these data to cavitation rheology results in porcine white matter.

2.3.2 Methods

2.3.2.1 Sample preparation

Half porcine brains (split sagittally through the center) were obtained from a local slaughterhouse within 1hr of sacrifice. Brain was immediately placed in Hibernate-A media, and kept on ice. The brain samples were sliced coronally to a thickness of 4-5mm with a razor and were cut into 25 mm diameter disks to fit the rheometer geometry. All measurements were conducted within 48 hours of sacrifice.

2.3.2.2 Rheology procedure

The procedure for rheology was described in Canovic et al.²⁵ Briefly, a parallel plate rheometer with a 25mm radius geometry was used to measure G' and G'' at 37°C, and sandpaper was adhered to both plates (320 grit, McMaster Carr) to prevent slip. Normal force was maintained at 0.01N, and was allowed to relax for approximately 5 minutes prior to rheology measurement. Samples were hydrated at the periphery with ~1m of Hibernate-A media.

Amplitude sweeps were used to determine that the linear viscoelastic range was within 2% shear strain. G' and G'' were measured at frequencies from 0.1 to 100 rad/s at 1% shear strain.

2.3.3 Results

Storage and loss moduli are shown in (Figure 2.4). G' was approximately 5 times higher than G'' , and both showed weak power laws with frequency. G'' increased more rapidly with frequency than G' . Additionally, G' and G'' increased with axial strain at all frequencies measured.

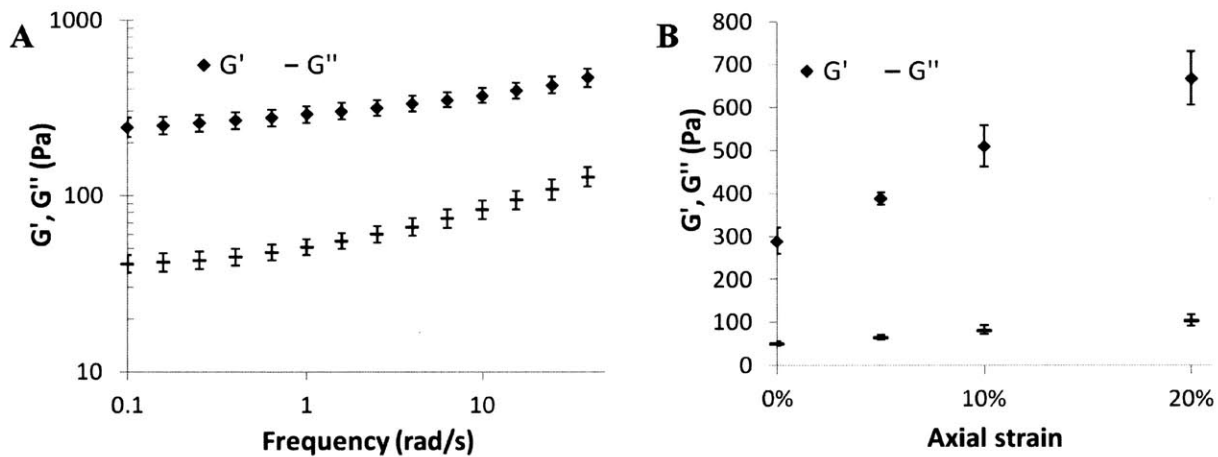


Figure 2.4: Rheology of porcine brain. (A) G' and G'' as a function of frequency show weak power laws ($N=4$). (B) G' and G'' vs. axial strain at 1rad/s. Both moduli increase with increasing axial strain, but G' increases more rapidly. Error bars represent standard deviation.

2.3.4 Discussion

Our measurements of G' and G'' match a number of studies in shear rheology for brain tissue, and can be compared with those shown in the review by Chatelin et al. (Figure 1.5).⁹ G' is on the order of hundreds of Pa, whereas G'' is on the order of tens of Pa. Both show increasing power laws, but G'' has a steeper slope; thus there is an increase in phase lag with frequency.

Additionally, we observed that G' and G'' increased when axial strain was applied (and thus stress state of the sample), but that G' increases more with axial strain than does G'' . The same trend was observed in a rheological study on mouse brain by Pogoda.³ This phenomenon highlights a limitation of rheology of compliant polymers and tissues: to have enough friction to obtain a reliable measurement, a normal force must be applied to the sample; however a normal force will cause a compressive pre-stressed/strained state in the sample, which, for nonlinear materials, will result in an altered measurement of modulus compared to an unstressed state. In this study and the previous measurements in **Section 2.2**, we consistently measured the mechanical properties under the same pre-stress. While this likely improved consistency between samples (for example, allowing for improved resolution between groups in **Section 2.2**) the mechanical properties were likely higher than would be expected in the state without pre-stress. This phenomenon is especially important to take into consideration for compliant samples, which may be axially compressed considerably prior to detection of axial force. For instance, our instrument has a sensitivity of up to 0.01N axial force.

We note that our sample was not homogeneous and isotropic due to the length scale of the measurement. Thus these measurements only give an average measurement of modulus, and are not capable of distinguishing between possible differences in stiffness in white vs. gray matter. Interestingly, the measurements are consistent between samples, resulting in a relatively small standard deviation (**Figure 2.4**). One explanation for this consistency is that samples had a similar proportion of white and gray matter. Additionally, while gray and white matter have different stiffnesses, white matter is less than two times stiffer than gray matter.^{1,21,26}

3 Cavitation rheology of mammalian brain tissue

3.1 Introduction

Many methods have been used to quantify the elastic modulus and viscoelastic moduli of brain, as described in **Section 1.2.4**. Different methods measure these properties on various length scales; for example, rheology operates on the macroscale, whereas atomic force microscope enabled indentation operates on the length scale of microns. There is much debate in the literature over the true value of elastic modulus of brain tissue, with measurements ranging several orders of magnitude between techniques, and even when a single technique is used.^{9,30} Cavitation rheology is a relatively new mechanical characterization technique that has been used to measure the elastic modulus of *ex vivo* tissues⁵⁵⁻⁵⁷ and compliant polymers⁵⁸⁻⁶⁰ on the length scale of hundreds of microns to a millimeter, and *in vivo* characterization of skin tissue has also been conducted. Measurement of local modulus of brain is relevant for study of disease and modeling of TBI (**Sections 1.1.1 and 1.1.2**). Prior to this study, the cavitation rheology technique has not been used to measure the elastic modulus of brain tissue.

3.2 Background

Cavitation rheology's use to measure Young's modulus has been demonstrated in compliant polymers as well as *ex vivo* and *in vivo* tissues.^{56,61,62} Its advantages include low cost, portability, ability to measure local mechanical properties, and ability to measure properties without preprocessing of the sample (e.g., slicing).^{59,61,62} Since mechanical properties of *ex vivo* tissues such as brain have been shown to change with time, this technique is a cheap alternative to magnetic resonance elastography for modulus measurement of *in vivo* tissues or intact *ex vivo* (e.g., bone marrow in the bone).⁵⁶

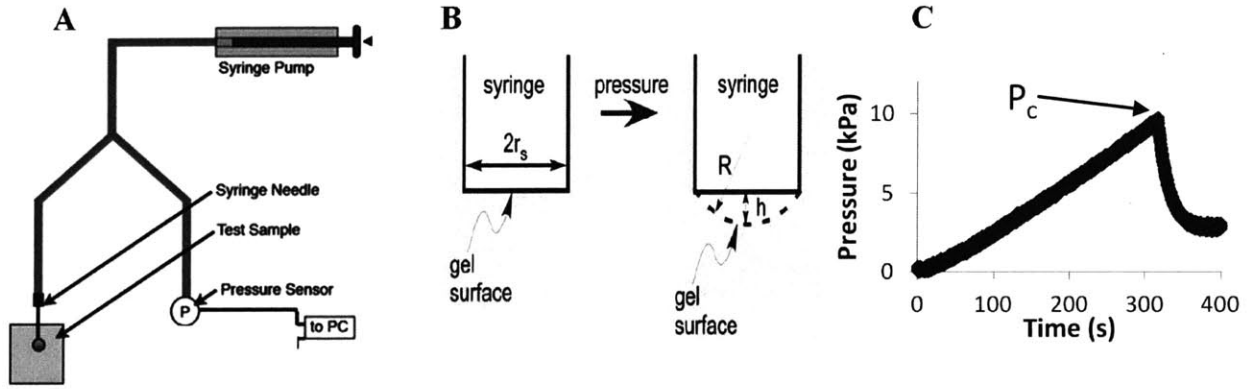


Figure 3.1: The cavitation rheology technique. (A) Experimental setup. A syringe needle is inserted into the test sample, and air is ramped through a syringe pump. Pressure vs. time is measured by a pressure sensor. (Adapted from Zimmerlin et al.⁵⁹). (B) As pressure is increased, a bubble is formed in the form of a spherical cap with a radius of curvature R and height h . (Adapted from Kundu et al).⁶⁰ (C) Raw pressure vs. time curve for porcine brain with an $80\mu\text{m}$ radius needle. The critical pressure P_c occurs at the maximum pressure.

In this technique, a fluid (e.g., air or water) is pressurized through a syringe needle, which is inserted into the polymer or tissue sample (**Figure 3.1**).^{55,59,60} The pressure is ramped at a constant rate with a syringe pump. The pressurization creates a bubble which slowly grows initially as the pressure is balanced by both surface tension and elasticity of the polymer or tissue (**Figure 3.1B**), but when the radius of the bubble exceeds the needle radius, surface tension resistance rapidly decreases with deformation. At a certain deformation, there is a maximum in the total resistance, and resistance to pressure begins to fall with deformation, causing unstable bubble growth, or cavitation (**Figure 3.1C**). For isotropic, neoHookean materials, this maximum pressure P_c may be related to the sample's Young's modulus E by

$$P_c \approx \frac{5}{6}E + \frac{2\gamma}{r} \quad (3.1)$$

where γ is the surface tension and r is the needle radius.^{59,60} This result is not exact, as it is obtained from the analytical solutions of (1) a pressurized spherical void in an infinite solid and (2) the surface tension of a spherical cap.⁶⁰ The geometry is clearly different than condition (1)

as the bubble forms a spherical cap, but taking into account these geometrical factors via finite element simulation has provided a very similar relationship:⁶³

$$P_c = 1.05E + \frac{2.1\gamma}{r} \quad (3.2)$$

Young's modulus may be determined with either of these equations by measuring P_c for different needle radii, and plotting the linear P_c vs $\frac{1}{r}$ curve. The slope of the line gives the surface tension, while the y-intercept gives the modulus.

As described previously, tissues and polymers often are viscoelastic and not hyperelastic. Pavlovsky showed that the viscoelastic effects may affect the P_c , but that viscoelasticity effects may be used in the analysis via imaging of the bubble and thus measuring strain rate over time.⁵⁸ However, from basic viscoelastic theory, a low enough strain rate would result in, for example, relaxed dashpots in the generalized Maxwell model, and thus the elastic response can be thought of as the relaxation modulus (**Section 1.2.1**). Further, fracture or yielding are instabilities which may also result in a critical pressure; in these cases, E cannot be calculated from P_c with the above analysis.⁶⁰

In this study, cavitation rheology in porcine brain is conducted for the first time, and these results are validated by rheology.

3.3 Methods

3.3.1 Brain samples

Porcine brains were obtained from a local slaughterhouse within 1hr of sacrifice and immediately placed in Hibernate-A media. Brain tissue was sliced with a razor into

approximately 2 cm thick slices for mechanical testing, and all measurements were conducted within 48 hours of sacrifice.

3.3.2 Cavitation rheology procedure

Prior to measurement, needles were calibrated by bubbling air in deionized water and measuring the pressure at which bubbles were formed. This pressure was compared to the critical pressure predicted by Laplace's law,

$$P_{c,w} = \frac{2\gamma_w}{r} \quad (3.3)$$

where r is the needle radius of the needle and $\gamma_w = 73$ mN/m is the surface tension of water at room temperature. This analysis assumes that the minimum radius of curvature of the bubble in water is equal to the inner radius of the needle. If the observed gauge pressure was within 5% of the predicted pressure $P_{c,w}$ the needle was used in the experiment.

Cavitation rheology was conducted as described previously.⁵⁹ A schematic of the setup is shown in **Figure 3.1**. A needle (26, 28, 30, 31, or 33 gauge, Hamilton Company, Reno NV) was inserted 2-3mm into white matter of the brain. Air was pressurized through a 20 mL syringe at a constant rate of (airflow rate) and thus (pressurization rate) via a syringe pump (PHD Ultra, Harvard Apparatus Holliston MA). Pressure was measured with a pressure sensor (PX26-005DV, Omega Engineering, Stamford, CN) and recorded in custom LabView program (National Instruments, Austin ,TX). The pressure vs. time curve for the tissue was obtained, and critical pressure was recorded (**Figure 3.1C**). Measurements were taken at different locations in the brain white matter and were at least 5mm apart. Five to 10 measurements were conducted for each needle radius used.

3.4 Results

To extract the modulus from the cavitation rheology data, critical pressure was plotted against the inverse of the needle radius. The data were fit with a linear model, and the elastic modulus was measured from the y-intercept, and the surface tension from the slope of the line, as seen by **Equation 3.2**. The average measurements for individual animals (**Figure 3.2A**) resulted in an average Young's modulus of 4.5 ± 2.8 kPa, and of all the animals pooled by needle radius (**Figure 3.2B**) a modulus of 4.7 kPa was obtained. As can be seen by the standard deviations in **Figure 3.2A**, there was considerable variability between measurements within individual animals; however, when the average critical pressures of animals were pooled, the measurements were relatively consistent and the standard deviation was considerably lower (**Figure 3.2B**).

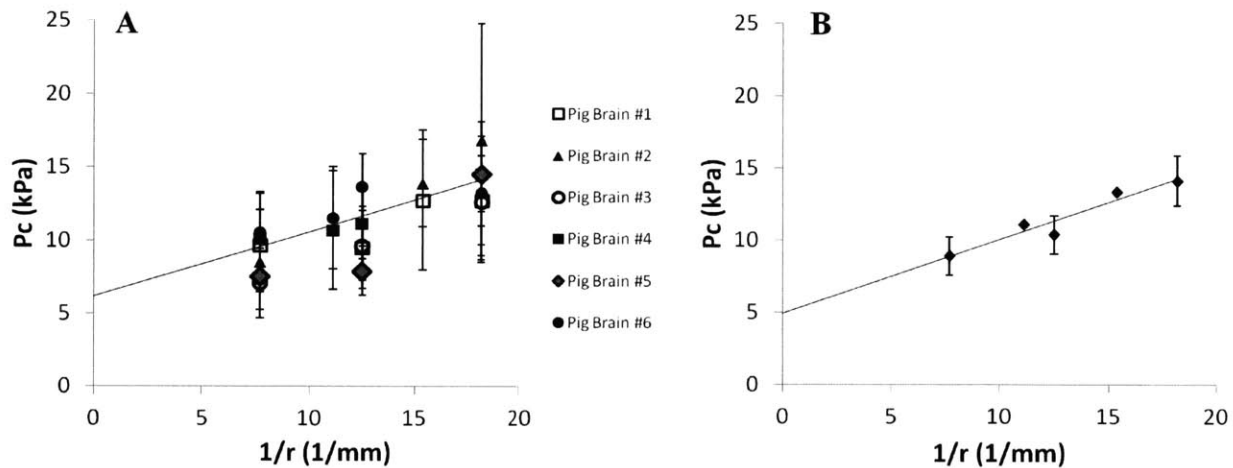


Figure 3.2: Cavitation rheology of porcine brain. Critical pressure vs. inverse needle radius for (A) individual porcine brain samples and (B) averaged measurements across animals at various needle radii. There is clearly much variability for measurements of individual animals, but the average measurements have less variability. Error bars represent standard deviation. Error bars are not included for points where $n < 4$.

Rheology of porcine brain was measured to validate these results (**Section 2.3**). When fit to a Prony series, these data gave a glassy modulus of $E_0 = 2700$ Pa and a relaxation modulus of

$E_{\infty} = 560$ Pa. These values are lower than that measured by cavitation rheology, but are within an order of magnitude.

3.5 Discussion

In this study, we demonstrated the first use of cavitation rheology for measuring the local Young's modulus of brain tissue. Although this technique may be used without sectioning the tissue, in the present study the brain was sectioned for convenience.

The white matter of the porcine brain was observed to have a modulus on the order of several kPa, which is in agreement with the range observed in the literature.³⁰ However, measurement of the same tissue with rheology showed that both the glassy and relaxation modulus were lower than the cavitation rheology value. These findings are consistent with studies in bovine eye and bone marrow, in which the observed Young's moduli were higher in cavitation rheology as compared to rheology, but within an order of magnitude of each other.^{55,56}

Based on theory, we would expect that the modulus measured by cavitation rheology would be closer to the relaxation modulus (**Section 1.2.1**), as the deformation was relatively slow (deformation took place), but since the pressure input was ramped, it is possible that the modulus measured was higher than the relaxation modulus. Experiments by Peyton et al. (unpublished, as part of this collaborative study) showed that increasing the rate of loading also changed the measured modulus. Future experiments and theoretical explanations should be done to determine appropriate pressurization rates for measurement of the relaxation modulus.

Part of the reason for this may be explained by the fact that only white matter was measured with cavitation rheology, whereas rheology measured both white and gray matter. Budday et al. and Johnson et al. showed that white matter was approximately 50% stiffer than gray matter; interestingly both studies had stiffer storage modulus values, on the order of kPa.^{1,26}

Another possibility is that a significant portion of the strain was in the nonlinear range, and that the neoHookean model does not have sufficient strain stiffening to capture the nonlinearity of brain tissue.

Cavitation rheology also measures surface tension. Interestingly, the value of 220 ± 100 mN/m obtained for brain was much higher than that of water (73 mN/m), the predominant component of the tissue composition. Bovine eye was found to have a similar surface tension value (200 mN/m)⁵⁵ and, while not explicitly reported in Jansen et al., the slope of P_c vs. $1/r$ for bone marrow yields approximately 200 mN/m.⁵⁶ Reported values for polyethylene oxide and poly(methyl methacrylate)-poly(*n*-butyl acrylate)-poly(methyl methacrylate) triblock gels are lower, on the order of 10's of mN/m.^{58,64} It is unclear why the surface tension value of brain tissue is higher than water, and why there is similar observed surface tension between different soft tissues.

A common problem with accurately measuring Young's modulus with cavitation rheology is fracture at the critical pressure. While fracture is easily identifiable from visually inspecting a deformed polymer,⁶⁰ fracture cannot be assessed for opaque tissues. Additionally, a critical pressure is observed whether the sample undergoes fracture or cavitation, so the dominant process is not visible from pressure vs. time data. A previous study in bovine eye suggested that cyclic pressurization of the tissue would suggest cavitation vs. fracture; cavitation is a reversible processes which would show consistent critical pressures with repeated cycles, while fracture is not reversible, and critical pressure would drop with cyclic loading.⁵⁵ Thus, our collaborators have conducted cyclic pressurization in murine brain tissue (**Figure 3.3**). These data show that, while the critical pressure drops for the first several cycles – which may indicate irreversible deformation – it remains essentially constant in subsequent cycles. The reason for

this drop in critical pressure with pressure cycling could be explained by preconditioning of the tissue, a phenomenon which has been observed in brain tissue (**Figure 1.6C**). However, future work visualizing the deformation would more clearly determine whether fracture or cavitation occurs in these experiments.

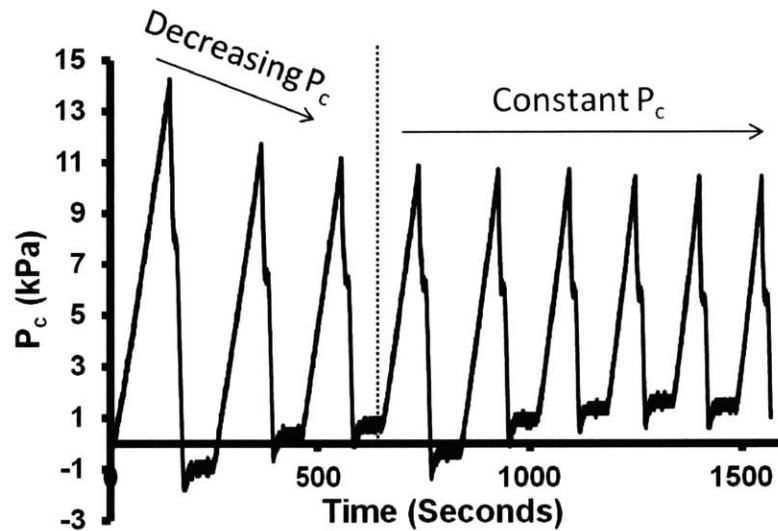


Figure 3.3: Repeated pressurization-depressurization cycles in murine brain tissue in a single location. Cavitation pressures appear to decrease with the first several cycles, but stay constant with subsequent cycles. It is unclear whether this decrease in cavitation pressure is due to preconditioning of the tissue or a failure mechanism. Unpublished data provided courtesy of Professor Shelly Peyton and Sualyneth Galarza.

4 Impact indentation of compliant viscoelastic materials: A new analytical framework and connection to other experimental techniques

4.1 Introduction

Impact indentation is an experimental technique recently developed by Van Vliet et al. that may be used to assess the impact response of compliant tissues and polymers.²³ Specifically it has been used in conjunction with shear rheology to mechanically characterize tissue simulant polymers, which are intended to have a similar mechanical response to soft tissues such as heart, liver, and brain.^{6,28} The technique involves the impact of a sample with a pendulum with a small (~mm) indenter tip, and the displacement vs. time response may be used to quantify the maximum penetration depth, quality factor of the oscillation, and the energy dissipation capacity of the material (see **Section 4.2.2**). One study using rheology and impact indentation showed a successful match of recently developed crosslinked PDMS-based gels to heart tissue, but an adequate match was not found for more compliant liver.⁶ A more recent study using impact indentation only has shown that multilayered composite gels match the impact response of brain tissue.²⁸

While the match between the impact response of the polymer to the response of the tissue is clear,^{6,28} the interpretation of these outcome measures and their relation to rheological measurements were only qualitatively understood. Comparison between impact indentation and rheology experimental data has been limited to qualitative changes (e.g., maximum impact depth decreases with increasing G').⁶ Moreover, the model for these experiments relied on finite element modeling in ABAQUS (Dessault Systèmes, Vélizy-Villacoublay, FR), which provided qualitative predictions and was only able to predict responses of impact indentation from rheology material properties, but not the inverse problem.

In this chapter, an analytical model for impact indentations is developed based on linear viscoelastic theory and contact mechanics. A direct relationship between rheology and impact indentation is developed, enabling improved understanding of how the material properties affect the impact response without the need for more time consuming finite element modeling. New relationships between impact indentation parameters are also established, and new numerical tools are introduced to fit the impact indentation raw data. Moreover, the inverse problem of relating impact indentation experimental data to rheological parameters (e.g., G' and G'') is solved and demonstrated via data simulated in ABAQUS.

4.2 Background

4.2.1 Simple mass spring dashpot system

The analysis in this section hinges on the analysis of a simple, one dimensional spring-mass-damper model of a mechanical system. From elementary dynamics, we know that

$$m\ddot{u} + b\dot{u} + ku = F(t) \quad (4.1)$$

where u represents displacement, m is mass, b is the damping coefficient, and k is the stiffness of the spring. Impacts may be modeled by a delta function in the external force term $F(t)$ with a magnitude equal to the impulsive force (equivalently one may set the force term as zero and input the velocity into the initial conditions); any other external loads on this system can be lumped in this term. The mechanical behavior of an impact response is based on the poles or eigenvalues of the system; the solution will be a damped oscillation in the form⁶⁵

$$u(t) = c_1 e^{\lambda_1 t} + c_2 e^{\lambda_2 t} \quad (4.2)$$

Where the eigenvalues are defined as:

$$\lambda_{1,2} = \frac{-b}{2m} \pm \sqrt{\left(\frac{b}{2m}\right)^2 - \frac{k}{m}} \quad (4.3)$$

It is convenient to rewrite this in terms of the “natural frequency” $\omega_n = \sqrt{\frac{k}{m}}$, and the damping ratio $\zeta = \frac{b}{2\omega_n m}$:

$$\lambda_{1,2} = \left(\frac{-b}{2m\omega_n}\right) \omega_n \pm \omega_n \sqrt{\left(\frac{b}{2m\omega_n}\right)^2 - 1} = -\zeta\omega_n \pm \omega_n \sqrt{\zeta^2 - 1} \quad (4.4)$$

If $\zeta < 1$, the system is underdamped, then we obtain the solutions:⁶⁵

$$\begin{aligned} u(t) &= c_1 e^{-\zeta\omega_n t + i\omega_n \sqrt{1-\zeta^2} t} + c_2 e^{-\zeta\omega_n t - i\omega_n \sqrt{1-\zeta^2} t} \\ &= c_1 e^{(-\alpha + i\beta)t} + c_2 e^{(-\alpha - i\beta)t} \end{aligned} \quad (4.5)$$

The quality factor of the system is defined as:

$$Q = \frac{1}{2\zeta} = \frac{\omega_n}{2\alpha} \quad (4.6)$$

and can be interpreted as the number of cycles it takes the amplitude of the system to decay by e .⁶⁵

4.2.2 Impact indentation experimental method

The impact indentation method may be used to measure the underdamped impact response of a viscoelastic material.²³ The method uses an instrumented nanoindenter (Micro Materials, Wrexham, UK) with a pendulum as the indenter or impactor (**Figure 4.1**). The sample is attached to the stage by glue and may be hydrated during the entire procedure. The impact procedure is as follows: First, contact is established such that the measurement frame is known. Next the pendulum is held in place by a solenoid while an electromagnetic force is applied (i.e., preloaded) at the top of the pendulum. When the pendulum is released, the load accelerates the

pendulum toward the sample, and the sample is impacted with the pendulum; the electromagnetic load is applied throughout the entire procedure. The displacement vs. time (and therefore velocity and acceleration) is recorded via capacitor plates at the bottom of the pendulum. Impact speeds on the order of 10s of mm/s have been achieved, and high strain energy densities may be achieved due to small indenter radii (on the order of a millimeter). Two indenter geometries have been used thus far: spherical and cylindrical flat punch.^{6,23} Gravity plays a role in the acceleration of the pendulum, but the magnitude and direction depends on the equilibrium position of the pendulum; this will be explored in **Section 4.4.9**.

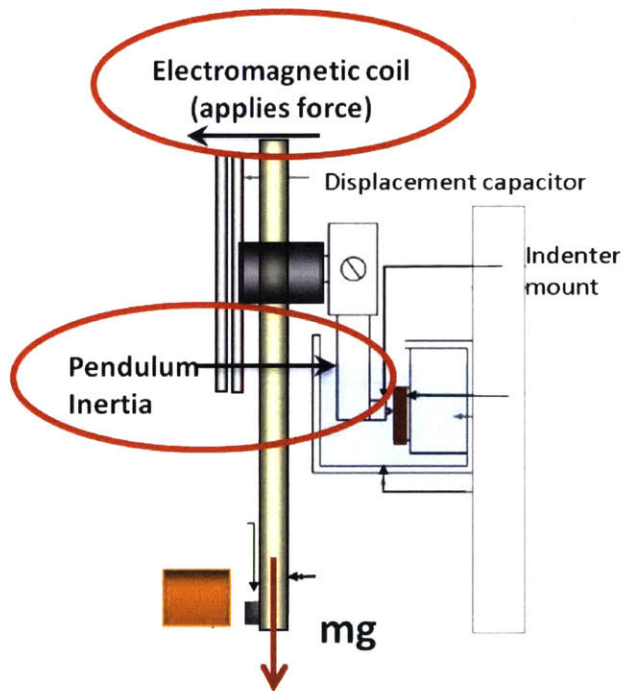


Figure 4.1: Schematic of the impact indentation device. A sample is mounted on the stage. The pendulum is accelerated toward the material and impacts with a small flat punch or spherical indenter. The three loads that are felt by the deformed material are (1) the pendulum inertia, (2) an electromagnetic force on the pendulum (which in turn applies load on the sample) and (3) gravity. Displacement vs. time is measured via capacitor plates.

4.2.3 Original analysis of impact indentation data

The analysis used in previous studies has relied on a mass-spring-dashpot model with a pure impact (i.e., the force term in **Equation 4.1** is a delta function).^{6,23,66} Three parameters were measured in the previous impact indentation studies: the maximum penetration depth x_{max} ; energy dissipation capacity K ; and the energy dissipation quality factor Q (**Figure 4.2**).^{6,23,25,28,66} The quality factor is the same as previously described, where Q was measured by fitting the exponential decay relaxation time of the top “envelope” of the curve (α in **Equation 4.6**) and the natural frequency, and calculated from **Equation 4.6** (**Figure 4.2A**).^{6,23,66}

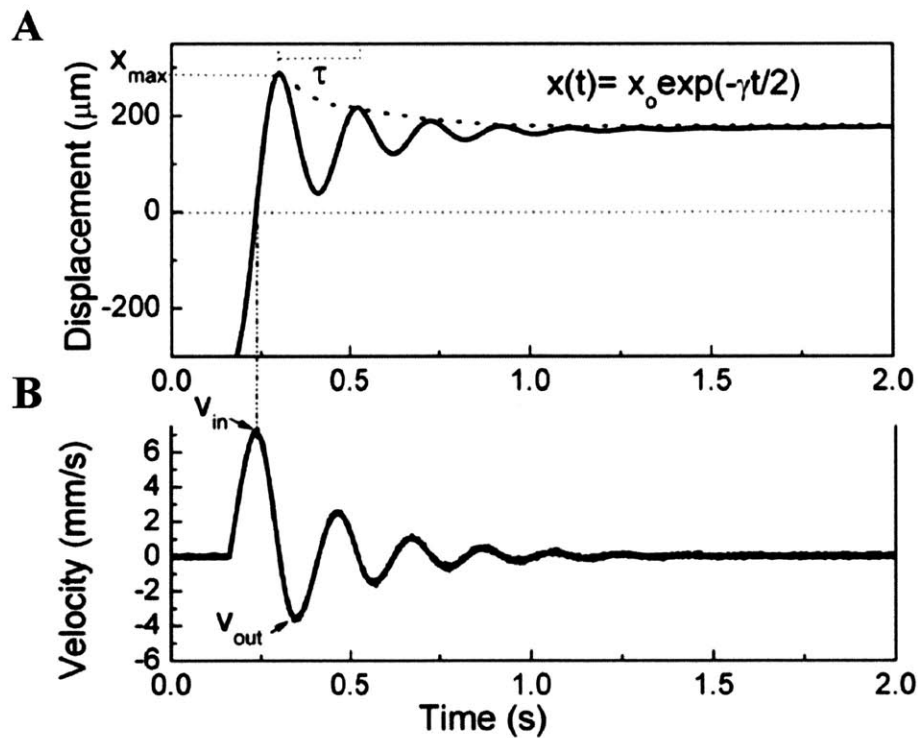


Figure 4.2: Raw experimental output and previous analysis in impact indentation. (A) Displacement vs. time and (B) velocity vs. time plots from an impact indentation experiment. x_{max} is found from the maximum displacement, K is measured from V_{in} and V_{out} , and Q is measured from fitting an exponential decay constant τ and from the frequency of the response. Adapted from Kalcioglu et al.²³

K is a measure of the total energy the material dissipates from impact for the first half cycle; it is measured from the kinetic energy in from the impacter $E_{in} = \frac{1}{2}mv_{in}^2$, the kinetic energy out of the impacter $E_{out} = \frac{1}{2}mv_{out}^2$, the energy dissipated by the pendulum E_d^p , and the energy stored due to pendulum “stiffness” E_r^p .²³

$$K = \frac{E_{in} - E_{out} - E_d^p - E_r^p}{E_{in} - E_d^p - E_r^p} \quad (4.7)$$

We note that the analysis for K and Q hinges on the assumption that the impact kinetic energy is the only significant energy inputted into the system.

4.2.4 Previous finite element modeling

A finite element model was created to help analyze these data, as well as to determine techniques to design tissue simulant polymers that match impact response of tissues.⁶⁶ The model described by Adityan⁶⁶ was used to help design polymers with the same impact response as tissues by altering parameters in the viscoelastic properties via altering the solvent loading, crosslinking of the material, etc. Additionally, a multilayer composite polymer system was used to better replicate brain tissue response to this mechanical impact loading.²⁸

This general approach to measure the system is appropriate for matching and customizing impact response of different materials. Even if the parameters are inaccurate in a general sense, if they are measured consistently between different samples, good matches for tissue simulant materials may be verified.

Nevertheless, several of the assumptions presented above are not valid, and the model accuracy must be improved to extract more meaningful parameters from the data (e.g., more accurate measures of Q or viscoelastic moduli). While the impact response was replicated by

simulation and experiment, it can be argued that the interpretation of the data is inaccurate and incomplete. A more rigorous analysis of the collected experimental data may yield more useful relationships. First, the interpretation of the data will be analyzed from a phenomenological level via simulation, showing the limitations of measuring K and Q as has been done previously. Next a new analytic technique will be proposed and validated by simulation. Additionally, relationships between the empirical parameters x_{max} , K and Q will be discussed, and a mathematical relationship between rheological data, impact indentation parameters, and frequency dependent moduli will be established.

4.3 Limitations of the previous model & data analysis: Effect of load on K and Q

In this section, we explore the effect of the experimental conditions on the calculation of K , Q and x_{max} via finite element simulation. In particular, we investigate the effect of the electromagnetic load (which is applied to the pendulum to accelerate it toward the sample) on these output parameters. This is of particular interest because the superimposed load is not taken into account in the previous calculations of K and Q , where an inertial impact (i.e., impulse input) is assumed. In studies we have published, we have assumed that K , Q and x_{max} were functions of impact velocity only, but experimentally, the impact velocity and the external magnetic load applied are coupled; the external load must be increased to increase the impact velocity. In simulation we are able to decouple these effects, and analyze the effect of individual variables.

We used a simplified model of impact loading in ABAQUS Standard (**Figure 4.3**), based on a previous model probe geometry and mesh.⁶⁶ In this simplified model, a mass impacts the viscoelastic material with a velocity V_{in} and with a superimposed load P , which are varied separately. For simplicity, we ignored the effects of adhesion, pendulum stiffness, pendulum

damping, and gravity, which have been incorporated in the previous finite element models. The viscoelastic material was defined by a Prony series which was fitted from rheological data; the constants of the Prony series are listed in **Table 1**. However, the relaxation was only assumed to occur in the shear modulus, but not the bulk modulus, contradicting previous analyses. The density of the viscoelastic material was 965 kg/m^3 , the mass of the impactor was 0.171 kg and the geometry of the indenter was a rigid flat punch of 1 mm radius, which has a beveled edge to improve numerical stability. ABAQUS Standard was used because the deformation was assumed to be quasistatic.

Table 1: Prony series of PDMS data used for ABAQUS simulation

$G_0 = 25.7 \text{ kPa}$	
Time constants $\tau_j \text{ (s)}$	Normalized Prony coefficients G_j/G_0
0.0412	0.63
0.340	0.089
0.702	0.0038
1.45	0.032
2.89	0.0077
5.88	0.013
11.9	0.012
24.9	0.0060
49.2	0.0018
100	0.0068

The raw data output for different responses of the system are shown in **Figure 4.3 B.i-iii**. **Figure 4.3 B.i.**, shows the response of an impact without a superimposed load, with the impactor-sample interface remaining in contact (black) and when contact may be lost (red).

When the two surfaces remain in contact, a damped oscillation analogous to the impulse response to a mass-spring-dashpot is observed; when the surfaces do not remain in contact, the impactor leaves the sample at a velocity V_{out} , which is constant after contact due to no external loading. **Figure 4.3 B.ii.** is the response of a step load P with no initial velocity; this is analogous to a creep experiment, except the system is underdamped, so oscillations are present. The displacement gradually reaches equilibrium, and contact is never lost. **Figure 4.3 B.iii.** is an impact with V_{in} and superimposed load P , identical to the ideal conditions assumed in impact indentation, neglecting pendulum stiffness, gravity, and pendulum damping; contact is not lost in this case, but may be lost when impact velocities are high comparing to superimposed load.

Next we consider how the superimposed load and impact velocity independently affect the energy dissipation capacity K (**Figure 4.4A**). To do so, we varied the impact velocity while keeping the superimposed load constant (**Figure 4.4A**). Additionally, the closed blue circles show the simulated data at experimentally relevant loads and impact velocities, and the open black circles show real experimental data at those same applied loads and impact velocities. x_{max} is similarly affected by the superimposed load (**Figure 4.4B**).

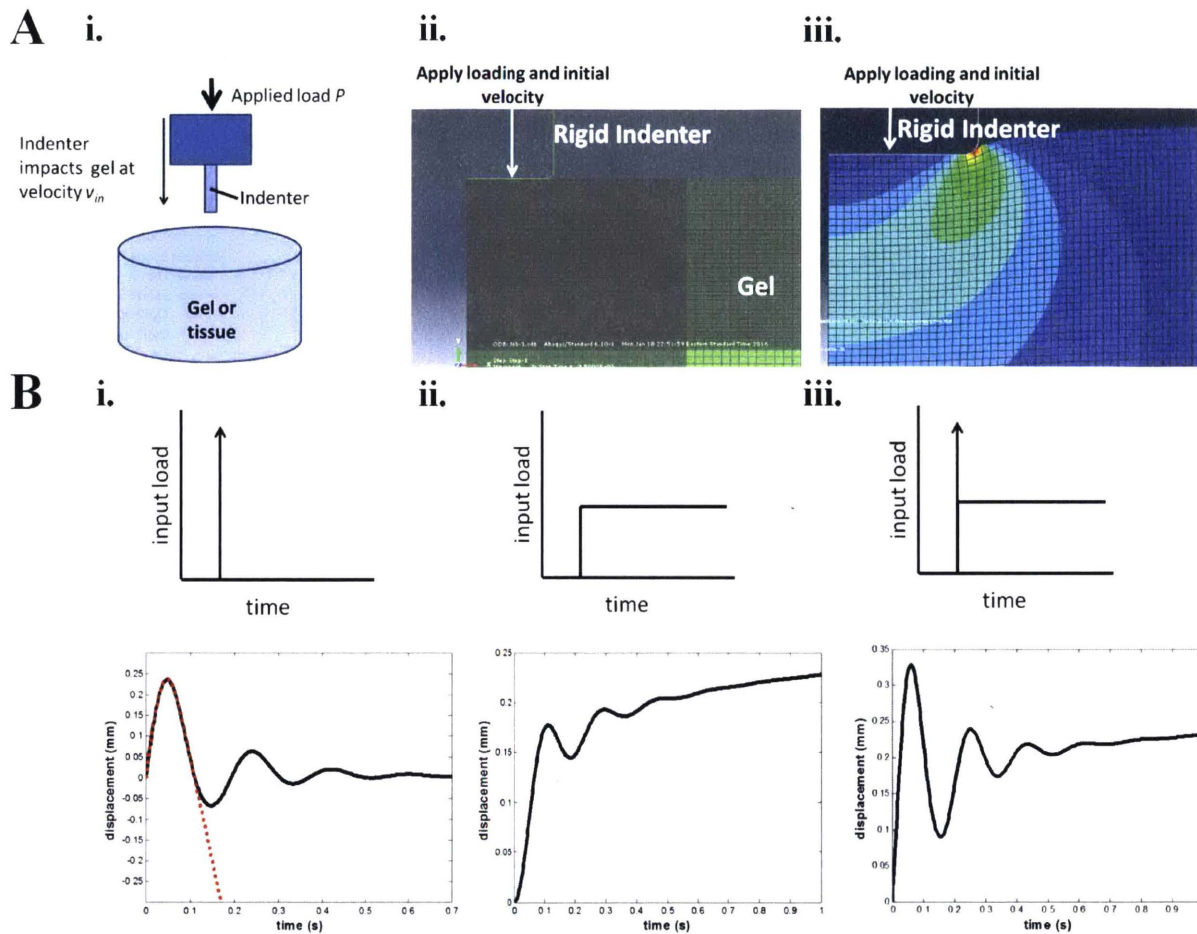


Figure 4.3: Finite element model of a simplified impact indentation experiment with various loading and velocity input conditions. (A) i. Cartoon representation of an impact indentation experiment neglecting gravity and pendulum damping. A rigid indenter with a mass m impacts a viscoelastic gel with a velocity V_m and external load P . ii. A 2-dimensional FEA model prior to impact. The mesh in the gel is concentrated near the impactor. iii. FEA model under impact with von Mises stresses shown. Stresses in the material are highest at the edge of the indenter (stress increases from blue, green, yellow to red). Since the deformation is quasistatic, no wave propagation is observed. (B) i. Pure impact. Impulse load input with impactor remaining in contact (black) and losing in contact (red). If the impactor remains in contact, the displacement vs. time is a pure damped oscillation; if contact is not maintained, the impactor loses contact with the sample prior to the second peak of the damped oscillation. ii. Step load input: “creep” of an underdamped system. iii. Impact indentation input: simultaneous impulse and constant load input results in superposition of responses in B.i. and B.ii.

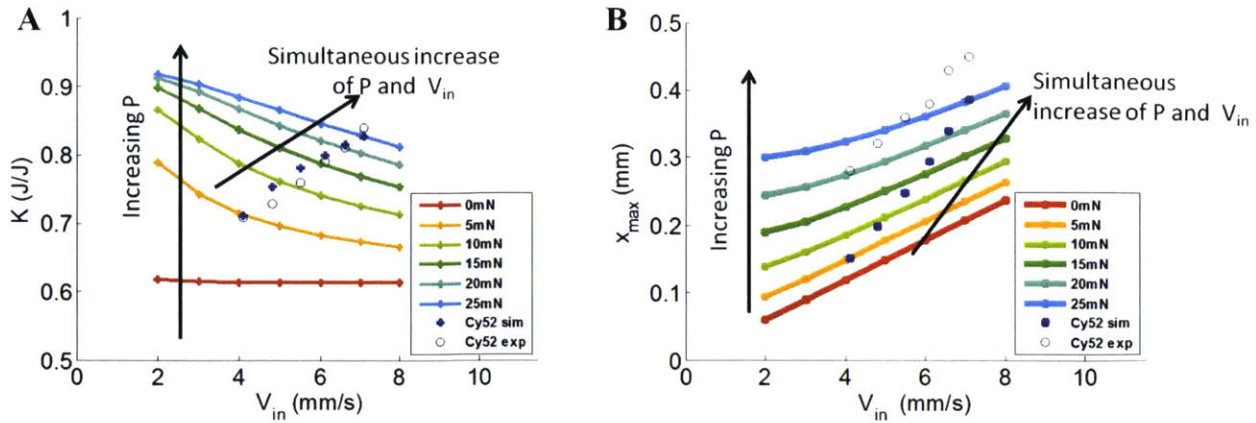


Figure 4.4: The effect of superimposed load on K and x_{max} . (A) K vs. V_{in} and (B) x_{max} vs. V_{in} for various constant external loads P (colored solid lines), simulated (closed circles) and experimental (open circles) data under experimental conditions. (A) For no load, K remains constant, while K appears to decrease with V_{in} for increasing load. (B) For no load, x_{max} increases linearly, and increasing load also increases. For the simulated and experimental data where V_{in} and load are coupled, the effect of the load and impact velocity are coupled.

We notice several trends. First, K is constant with impact velocity for pure inertial impact (no superimposed load). This is expected (and will be shown rigorously in the next section), as we are using a linear viscoelastic material model, so the energy dissipated is linearly related to the energy inputted; thus the energy dissipated normalized to the energy put in is constant. Next, we see that K increases as constant load increases. This is an artifact from normalizing to the energy inputted from the impact, but we are not taking into account the work done by the electromagnetic external load. It also explains the decreasing trend with increasing impact velocity with constant nonzero external load: the trend with impact velocity is an artifact due to normalizing data not to total energy inputted, but rather to the impact kinetic energy only. We also see that the K increases with V_{in} for both the simulated experimental conditions (blue closed circles), as well as with the experimental data (open circles). This trend could be attributed to the impact velocity coupled with increasing load and an incorrect method of normalizing the data.

Another way to interpret this effect of the external load is that K is being measured via the conservation of energy, where the energy inputted is only from the kinetic energy of the impactor; however, in reality the kinetic energy of the impactor is modulated because the electromagnetic load is also doing work on it, which decreases the kinetic energy of the pendulum in the rebound velocity of the impact. In other words, according to linear viscoelasticity, variation of K with impact velocity is an experimental artifact. Nonlinear material properties may also affect the energy dissipated, but the strain stiffening will tend to decrease energy dissipated with increasing impact velocity because the material behaves more elastically; the opposite trend is observed experimentally with the previous data analysis model.

Further, the analysis from **Equation 4.6** is also insufficient for measuring the quality factor Q for the system for essentially the same reason. Measuring Q by fitting a decaying exponential to the displacement vs. time curve and measuring the natural frequency of the material is only valid if the input function is an impulse (i.e., an inertial impact with no external loads). The external load drives the probe into the material, resulting in a final equilibrium point inside the sample. If the impact plane is plotted in the decayed oscillation, it is clear that one cannot draw two identical exponential decays that envelope the decaying oscillation (**Figure 4.2**), and it is this single time constant (along with the natural frequency of the material) that defines Q . Increasing the load will thus increase the time constant of the exponential decay on the top curve (which has been used to measure Q in all previous analysis) thus decreasing Q . Conversely, the bottom decay curve would result in an increased time constant with increasing load, further showing the inconsistency in the analysis. It is shown in these simulations and in experimental data that Q decreases with impact velocity, which is clearly due to the coupling with the electromagnetic load. However, in **Section 4.4.6** we will develop two new methods for

measuring Q from experimental data, and both clearly show that Q is constant with impact velocity when constant load is accounted for.

There may be regimes where this effect can be ignored (i.e., low external load, high impact force), but the results suggest that the compliant tissues of interest are in the regime where a conservation of energy analysis is not valid. To summarize: The data presented in various papers shows that K and Q are a function of impact velocity.^{6,23,28} The theory of linear viscoelasticity predicts that these parameters should be constant with impact velocity, and will be demonstrated rigorously in the following section.

Finally, K and Q are both system parameters, meaning that they are affected by the mass and geometry of the pendulum, as can be seen from **Equations 4.4** and **4.6**. A more exact relationship between mass and K and Q will be discussed in the following section.

4.4 A new analytic model of impact indentation

In this section we discuss an analytic viscoelastic model for impact indentation, and use it to (1) predict impact response from rheological data, (2) determine material properties from impact indentation data, (3) relate K and Q , and (4) establish further relationships between variables.

4.4.1 The relationship between K and Q

Q is a measure of the rate of dissipation of energy per unit cycle (natural frequency), and K is the amount of energy dissipated from impact to exit (approximately half a cycle). Clearly these two quantities should be related. A simple relationship may be established by assuming the solution of displacement of the impacter to be in the form of **Equation 4.5**. For an

impact at velocity V_{in} without external loading, the initial conditions are $u(t = 0) = 0$ and

$$\frac{du}{dt}(t = 0) = V_{in}:$$

$$\begin{aligned} u(t) &= \frac{V_{in}}{\omega_n \sqrt{1 - \zeta^2}} e^{-\zeta \omega_n t} \sin(\omega_n \sqrt{1 - \zeta^2} t) \\ &= \text{Im} \{ C e^{(-\zeta \omega_n + i \omega_d)t} \}, \end{aligned} \quad (4.8)$$

$$\text{where } C = \frac{V_{in}}{\omega_n \sqrt{1 - \zeta^2}} \text{ and } \omega_d = \omega_n \sqrt{1 - \zeta^2}$$

Taking the derivative of the complex displacement we obtain:

$$\frac{du^*(t)}{dt} = C(-\zeta \omega_n + i \omega_d) e^{(-\zeta \omega_n + i \omega_d)t} \quad (4.9)$$

The velocity over time is:

$$\frac{du(t)}{dt} = \text{Im} \left\{ \frac{du^*(t)}{dt} \right\} = C e^{-\zeta \omega_n t} [\omega_d \cos(\omega_d t) - \zeta \omega_n \sin(\omega_d t)] \quad (4.10)$$

If we assume that velocity out of the system occurs at time $t \approx \frac{T}{2} = \frac{\pi}{\omega_d}$ (this is not strictly true),

we see that:

$$V_{out} = \frac{du(t = \frac{T}{2})}{dt} = C e^{-\zeta \omega_n t} [\omega_d \cos\left(\omega_d \frac{T}{2}\right) - \zeta \omega_n \sin\left(\omega_d \frac{T}{2}\right)] \quad (4.11)$$

$$V_{out} = V_{in} e^{-\zeta \pi}$$

If we ignore the effect of the pendulum damping and stiffness, then the energy dissipation capacity reduces to:

$$K = \frac{E_{in} - E_{out} - \frac{1}{2}mV_{in}^2 - \frac{1}{2}mV_{out}^2}{E_{in} - \frac{1}{2}mV_{in}^2} \quad (4.12)$$

$$K = \frac{V_{in}^2 - V_{out}^2}{V_{in}^2} \approx 1 - e^{-2\pi\zeta}$$

$$K \approx 1 - e^{-\frac{\pi}{Q}} \quad (4.13)$$

A more exact solution for the same model may be obtained by solving for the maximum velocity, which is slightly before $t = \frac{T}{2}$ due to phase lag. The exact occurs at:

$$t = \frac{\pi}{\omega_d} - \tan^{-1} \left(\frac{\zeta(1-\zeta)^2}{-2\zeta+1} \right) = \frac{\pi}{\omega_d} - \delta(\zeta) \quad (4.14)$$

$$K = 1 - e^{-\frac{\pi - \delta(Q)}{Q}} \quad (4.15)$$

We observe that K may still be represented as a function of only Q . We note that this is only an approximation of the real system, as the transients were neglected in this analysis. Moreover, these expressions are only valid for geometries where the surface area of contact is constant. For the spherical geometry, for example, there is no close form solution in terms of elementary functions.

4.4.2 Quantifying x_{max}

If we use the same assumed solution for the displacement as **Equation 4.8**, we see that the maximum penetration depth x_{max} scales linearly with impact velocity V_{in} with a slope of $\frac{1}{\omega_n \sqrt{1-\zeta^2}}$. Clearly, x_{max} occurs when $\frac{du(t)}{dt} = 0$. If we assume that occurs at $t \approx \frac{T}{2} = \frac{\pi}{\omega_d}$

$$x_{max} = \frac{V_{in}}{\omega_n \sqrt{1 - \zeta^2}} e^{-\zeta \omega_n \frac{\pi}{\omega_d}} \sin\left(\omega_d \left(\frac{\pi}{\omega_d}\right)\right) \quad (4.16)$$

$$x_{max} \approx \frac{V_{in}}{\omega_d} e^{-\frac{\zeta \pi}{\sqrt{1 - \zeta^2}}} \approx \frac{V_{in}}{\omega_d} e^{-\frac{\pi}{2Q}} \quad (\text{when } 1 - \zeta^2 \approx 1) \quad (4.17)$$

4.4.3 A differential equation for impact on a viscoelastic material

Impacts on viscoelastic materials by rigid impacters have been investigated previously.^{67,68} In our experimental method, impacts tend to be in the quasistatic regime, where inertia of the viscoelastic material may be neglected, and therefore wave propagation effects can be ignored. The justification for this is that the timescales of impact (i.e., the period ~ 100 s of ms in the simulations above) are much longer than the time for the shear wave to propagate from the impacter and back (as the wave speed will be on the order of m/s for a material with a shear modulus of a kPa).⁶⁹ The simple mass-spring-dashpot system is often inadequate due to frequency dependence of viscoelastic materials and geometric effects of contact mechanics. The viscoelastic model we use is the generalized Maxwell model, which may be determined by fitting the rheological parameters $G'(\omega)$ and $G''(\omega)$, and may be rewritten in the time domain via the Prony series $G(t)$ (**Section 1.2.1**).

The one-dimensional (1D) impact of a rigid indenter and a viscoelastic material, as well as the impact of a spherical impacter, have been investigated thoroughly.^{67,68} In this section we apply this analysis to the impact indentation technique, and derive equations that may be applied to predict impact response via rheology data. Further, we use these equations with a systems analysis approach to relate rheological parameters and impact indentation results via transfer functions (**Figure 4.5**). We demonstrate the ability to use this analysis to measure glassy and

relaxation moduli from impact indentation data. The effect of pendulum gravity and constant applied electromagnetic load may be taken into account using this analysis.

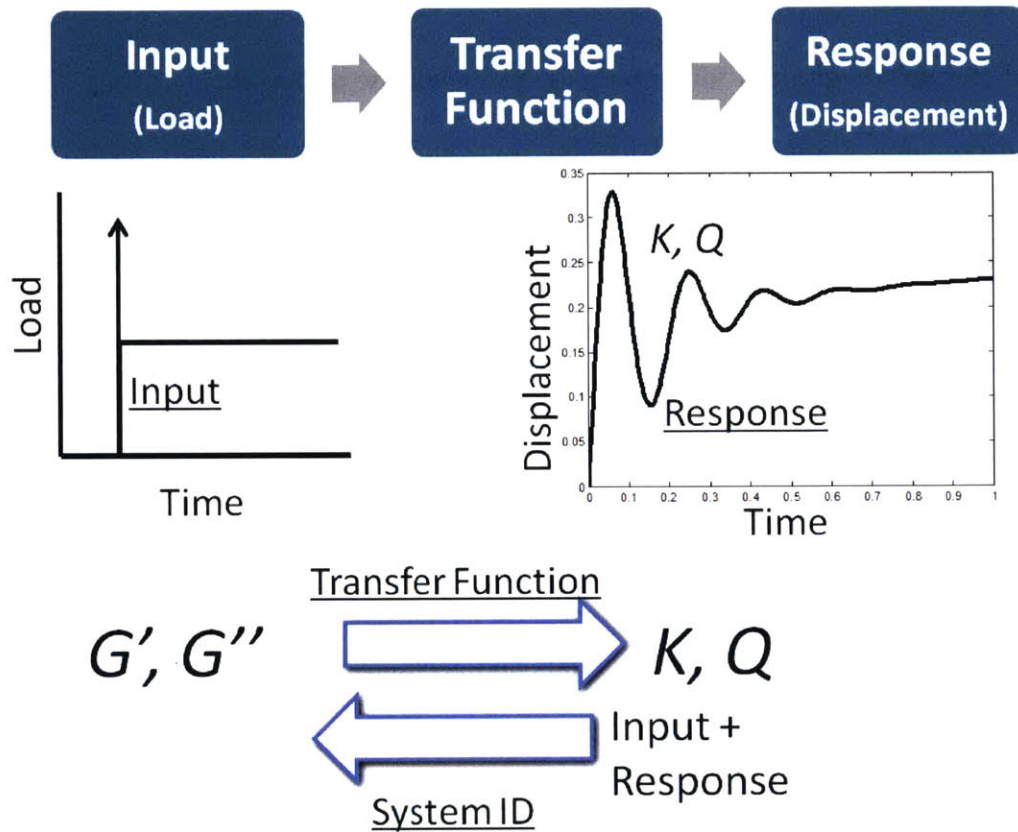


Figure 4.5: Relating rheological parameters to impact response. Transfer functions may be used to go from load vs. time input to displacement vs. time output, as well as to predict K and Q from rheological parameters. They may also be used to measure viscoelastic moduli from displacement vs. time output, which was not possible using finite element models.

Chen and Lakes present an excellent review of solutions for the impact of viscoelastic materials.⁶⁸ We note that we assume that inertia in the viscoelastic material is small comparing to that of the rigid impactor (i.e., the mass of the indenter is much larger than the mass of the viscoelastic material). We start with the purely linear elastic case. For 1D impact via a block indenter, the deformation over time can be described by the ordinary differential equations:

$$F(t) = m \frac{d^2u(t)}{dt^2} \quad (4.18)$$

$$m \frac{d^2u(t)}{dt^2} = -\frac{EAu(t)}{h} \quad (1D \text{ block impacter}) \quad (4.19)$$

where $u(t)$ is the displacement of the impacter, m is the mass of the impacter, E is the Young's modulus of the elastic material, A is the surface area and h is the thickness of the viscoelastic material.

$$m \frac{d^2u(t)}{dt^2} = -\frac{8R^{1/2}Gu^{3/2}(t)}{3(1-\nu)} \quad (\text{Spherical impacter}) \quad (4.20)$$

where R is the radius of the probe, G is the shear modulus, and ν is the Poisson's ratio. We note that **Equation 4.20** resembles the Hertz solution.⁶⁹ By analogy, using the static contact mechanics solution described by Johnson, we may express the impact of a rigid cylindrical flat punch indenter as:⁶⁹

$$m \frac{d^2u(t)}{dt^2} = -\frac{4RGu(t)}{(1-\nu)} \quad (\text{Flat punch impacter}) \quad (4.21)$$

Chen and Lakes go on to show that the impact of a viscoelastic solid for the rigid 1D block and spherical impacters, the governing differential equation may be written in terms of convolutions of the Prony series $E(t)$ or $G(t)$:⁶⁸

$$m \frac{d^2u(t)}{dt^2} = -\frac{A}{h} \int_0^t E(t-t') \frac{du(t')}{dt'} dt' \quad (1D \text{ block}) \quad (4.22)$$

$$m \frac{d^2u(t)}{dt^2} = -\frac{8R^{1/2}}{3(1-\nu)} \int_0^t G(t-t') d(u^{3/2}(t')) \quad (\text{Spherical impacter}) \quad (4.23)$$

Again, by analogy, it is clear the contact mechanics result for a flat punch indenter on a viscoelastic material may be used to model the impact as well:⁷⁰

$$m \frac{d^2 u(t)}{dt^2} = -\frac{4R}{(1-\nu)} \int_0^t G(t-t') \frac{du(t')}{dt'} dt' \quad (\text{flat punch impact}) \quad (4.24)$$

We note that the response of these solutions is only valid while the probe and the material are in contact. For the linearly elastic case, the impactor and the elastic material are in contact for exactly half a cycle, and for the viscoelastic case, contact will occur for slightly less than half a cycle. If a load is applied, then the situation may change and these instances are discussed later.

4.4.4 Solutions to “pure impact”: New analytic methods for Q

The solutions to **Equations 4.22, 4.23** and **4.24** may be found numerically. However, for the linear ODEs **Equations 4.22** and **4.24**, using transfer functions we can very easily calculate Q (and K from Q) without solving the solution (**Figure 4.5**). If we add an arbitrary force term $F(t)$ to the right hand side of **Equation 4.24**, divide through by mass m , and take the Laplace transform we obtain:

$$s^2 \bar{U}(s) + \alpha s \bar{G}(s) \bar{U}(s) = \frac{\bar{F}(s)}{m} \quad (\text{flat punch impact}) \quad (4.25)$$

Where

$$\alpha = \frac{4R}{m(1-\nu)}$$

Taking the Laplace transform of the Prony series (**Equation 1.3**) with n coefficients and substituting, we obtain:

$$s^2 \bar{U}(s) + \alpha \left(G_\infty + \sum_{i=1}^n \frac{G_i s}{s + 1/\tau_i} \right) \bar{U}(s) = \frac{\bar{F}(s)}{m} \quad (\text{Flat punch impact}) \quad (4.26)$$

We may obtain a solution in the form:

$$\bar{U}(s) = \frac{\bar{F}(s)}{\bar{P}(s)} \quad (4.27)$$

where the characteristic polynomial $\bar{P}(s)$ is:

$$\bar{P}(s) = m \left[s^2 + \alpha \left(G_\infty + \sum_{i=1}^n \frac{G_i s}{s + 1/\tau_i} \right) \right] \quad (\text{Flat punch impacter}) \quad (4.28)$$

If we set $\bar{P}(s) = 0$ we may solve this expression numerically to obtain the $n+2$ poles for the system, of which two are complex and n are real. The two complex poles are analogous to those in **Equation 4.4** and may be used to obtain Q . From Q we may obtain K (and x_{max}). The remaining n poles are transients from the relaxation times in the Prony series.

Thus if we can obtain the Prony series from rheological experiments and we know the mass and radius of a flat punch indenter, we may predict the impact response. We have reduced what was previously achieved by finite element model in **Section 4.3** to solving an algebraic expression. However, this analysis is only valid for the flat punch geometry, which we have used more extensively. The spherical indenter does not have solutions in terms of elementary functions, but may be solved numerically (**Equation 4.23**). This solution is an improvement over finite element analysis.

The forcing term for impact indentation experiments can be assumed to be a linear superposition of a Dirac delta function δ_d at contact time t_0 and a constant (electromagnetic) load F_{el} stepped at contact:

$$F(t) = \frac{mV_{in}}{\Delta t} \delta_d(t - t_0) + F_{el}H(t - t_0) \quad (4.29)$$

where $H(t - t_0)$ is the Heaviside step function and Δt is the time of impact.

4.4.5 A technique for measuring viscoelastic moduli by impact indentation

We now look to applying this simplified model of impact indentation to measure dynamic moduli by impact indentation, which is the inverse problem of that solved in the previous section (**Figure 4.5**). We notice that if it is possible to calculate the poles of the system from a known Prony series, it should also be possible to calculate the Prony series from poles (or corresponding transfer function), provided there are the same number of equations and unknowns. For the standard linear solid (i.e., one time constant in the generalized Maxwell model) the transfer function reduces to a 3rd order polynomial, and the three material properties (glassy modulus G_0 , relaxation modulus G_∞ , time constant τ) can be determined by solving the reduced **Equation 4.28**:

$$P(s) = m \left[s^2 + \alpha G_\infty + \frac{\alpha (G_0 - G_\infty) s}{s + 1/\tau} \right] \quad (4.30)$$

$$0 = s^3 + \frac{s^2}{\tau} + \alpha s G_0 + \alpha \frac{G_\infty}{\tau}$$

For a Prony series with more time constants, the analysis becomes more difficult. For a two term Prony series, there are five material properties: glassy or relaxation modulus (G_0 & G_∞), two time constants (τ_1 and τ_2), and two weights for time constants (G_1 & G_2), but only four poles.

$$P(s) = m \left[s^2 + \alpha \left(G_\infty + \frac{G_1 s}{s + 1/\tau_1} + \frac{G_2 s}{s + 1/\tau_2} \right) \right] = 0 \text{ (Flat punch impactor)} \quad (4.31)$$

In this case another parameter must be measured to obtain the five parameters. For example, in addition to the four poles, the relaxation modulus may be obtained from the depth of the probe as $t \rightarrow \infty$ (i.e., equilibrium is reached).

4.4.6 Methods for determining the poles from experimental impact indentation response: Logarithmic decrement and systems identification

To improve our measurement of the impact indentation parameter Q , two new data analysis procedures are explored: logarithmic decrement and systems identification. Logarithmic decrement is a very simple way of measuring the poles of a mass-spring-dashpot system, whereas systems identification may be used to fit data with transfer functions with as many poles for given input loading conditions.

Logarithmic decrement may be used to measure the damping coefficient of an underdamped system by measuring the values of the peaks of the damped oscillation. The logarithmic decrement Δ is defined as:⁶⁵

$$\Delta = \frac{1}{n} \ln \frac{x(t)}{x(t+nT)} \quad (4.32)$$

Where $x(t)$ is a peak, n is the number of periods between peaks, and T is the period. The damping factor is related to Δ by:

$$\zeta = \frac{1}{\sqrt{1 + \left(\frac{2\pi}{\Delta}\right)^2}} \quad (4.33)$$

And therefore the quality factor can be determined directly by the following relation:

$$Q = \frac{1}{2} \sqrt{1 + \left(\frac{2\pi}{\Delta}\right)^2} \quad (4.34)$$

$$Q \approx \frac{\pi}{\Delta}, \text{ when } \zeta \ll 1 \quad (4.35)$$

The convenience of this method of calculating Q is that it will calculate the same for impulse input, step input, and a combination of the two, provided that the system behaves like a simple mass-spring-dashpot system. This can easily be verified, and is provided in the

Appendix (and we note that a modified form of **Equation 4.32** must be used). Practically speaking, the constant load that complicated the previous analysis discussed in **Section 4.3** does not affect logarithmic decrement analysis. Moreover, the logarithmic decrement can be measured from the output data alone; the input signal (i.e., impact force, external load) is not necessary for the analysis.

A more complete picture of the poles can be provided from systems identification methods, as may be done with MATLAB's System Identification Toolbox (Mathworks, Natick, MA). Systems identification takes input and output data for a system and fits a prescribed transfer function (**Figure 4.5**). The fit and coefficients for the transfer function are measured, and the poles can be determined numerically from the characteristic polynomial.

4.4.7 Measuring material properties from impact indentation data: Proof of concept

In this section we use the methods in **Sections 4.4.3** and **4.4.6** to analyze data from simulated impact indentation data. The model used is the same as that of **Equation 4.24**, and like that model, the effects of gravity and pendulum damping were neglected. Material properties for a three component generalized Maxwell model (i.e., standard linear solid) were simulated to test the robustness of the analytical techniques to complexity of the true material properties.

4.4.7.1 Predicting impact response

Impact response can be predicted by measuring the displacement vs. time response via simulation in finite element software or solving **Equation 4.24**, or alternatively by calculating the poles of the system (i.e., the roots of **Equation 4.28**). The displacement vs. time response of ABAQUS simulation and numerical solution of **Equation 4.24** or **4.28** is shown in **Figure 4.6**. In these simulations, impact velocity was $V_0 = 4.1\text{mm/s}$, the constant force $P = 5\text{mN}$ with a

standard linear solid viscoelastic material of $G_\infty = 5.03$ kPa, $G_0 = 10.1$ kPa, $\tau = 0.05$ s, and $\nu = 0.49$.

A similar response is observed with the ABAQUS simulation vs. the numerical solution (Figure 4.6), but there is a clear disparity between the two, and the reason why is unclear. In theory, the two solutions should be identical, as both are based on the same material model, system properties, and loading conditions. One explanation for the discrepancy may be the beveled edges in the impactor in the finite element simulation, which are incorporated into the model for numerical stability.

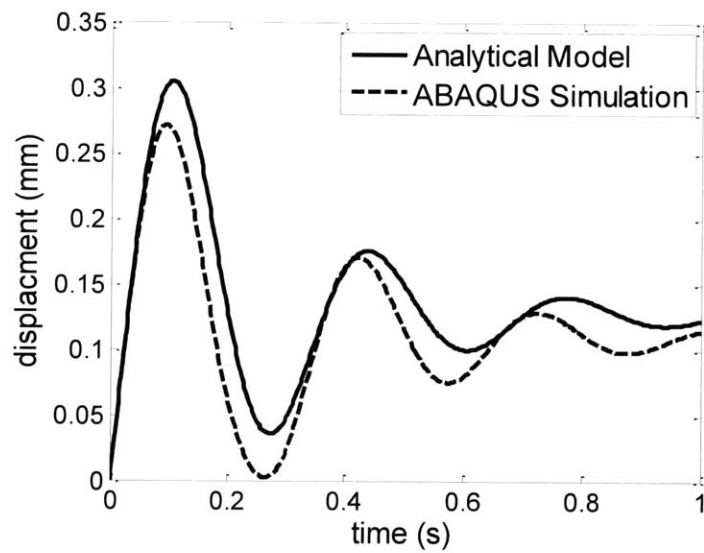


Figure 4.6: Displacement vs. time for a simplified impact indentation experiment simulated by an analytical model and in ABAQUS.

4.4.7.2 Analysis of simulated experimental data with logarithmic decrement: Measuring Q

The displacement vs. time responses of finite simulation and numerical simulation were analyzed via logarithmic decrement, from which Q was measured. The results are plotted against impact velocity in Figure 4.7. Unlike in previous analyses of K or Q , where these output measures were a function of velocity, logarithmic decrement shows that Q is a constant with

velocity (and applied load), as is predicted from linear viscoelasticity of a mass-spring-dashpot system. Interestingly, the constant Q value appears to hold when transients are included as well (this model includes relaxation times), at least in the range of impact velocities and loads that were evaluated here. **Equation 4.30** predicts a Q value of 2.53, showing that logarithmic decrement accurately measures Q .

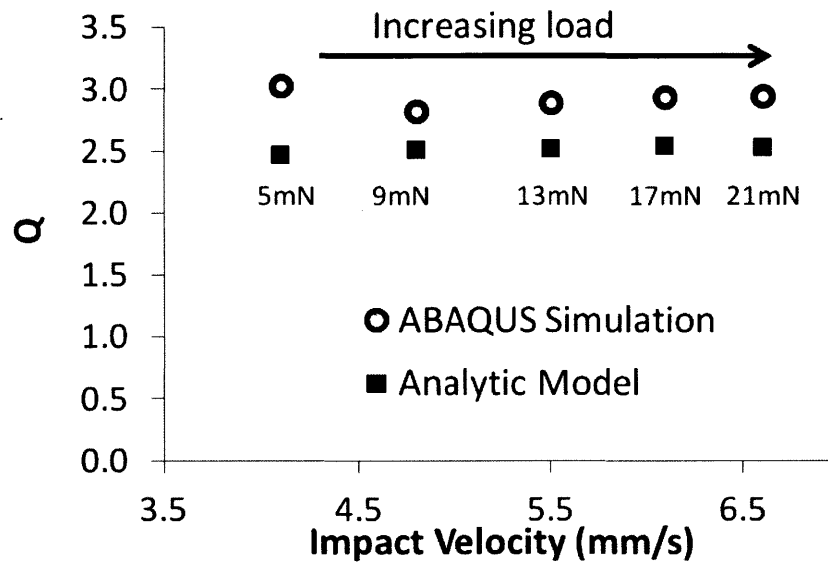


Figure 4.7: Q vs. impact velocity for ABAQUS simulation and analytic model output. Q was measured using logarithmic decrement. Measured Q is constant with impact velocity and with increasing load.

4.4.7.3 Analysis of simulated experimental data with systems identification: Measuring Q and viscoelastic moduli

Systems identification allows us to not only accurately measure Q , but to obtain enough information from the system to measure viscoelastic moduli and time constants, provided that experimental parameters such as mass and pendulum damping are known. In this analysis force vs. time and displacement over time are provided as input, and an assumed transfer function is fitted in the frequency domain. A fit of simulated data with the corresponding transfer function is provided in **Figure 4.8**. The coefficients of the transfer function or the roots of the characteristic

polynomial may be used to solve for G_∞ , G_i , and τ_i by solving a system of nonlinear equations in the form of **Equation 4.30** or **4.31**. **Table 2** shows that G_∞ , G_0 and τ may be accurately measured via systems identification.

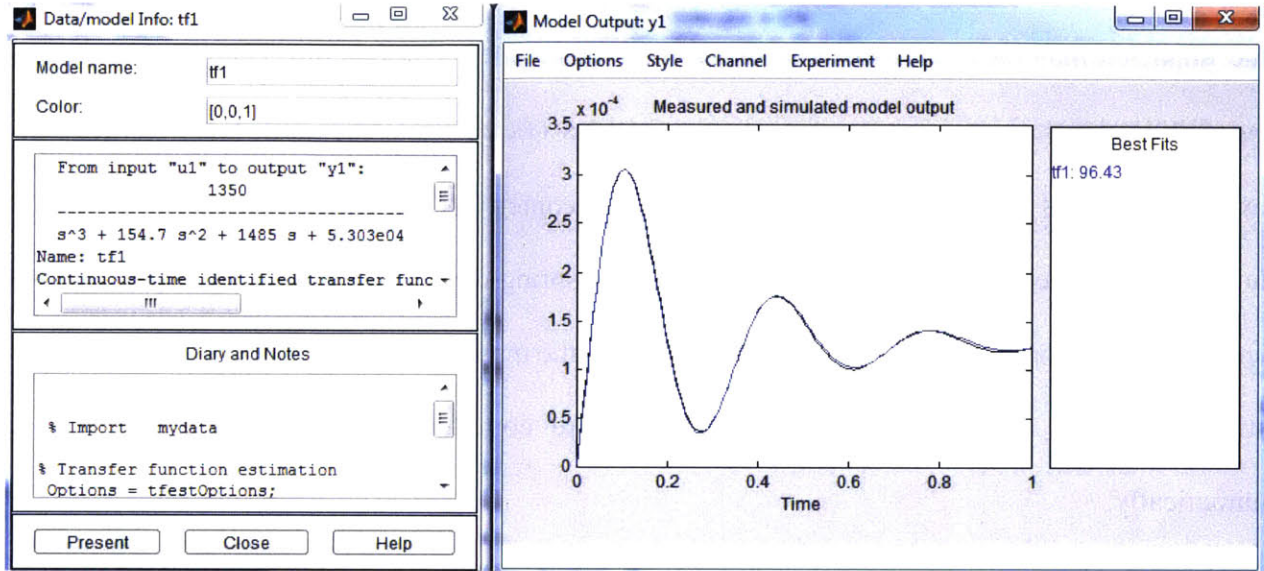


Figure 4.8: Systems identification of impact indentation data. Fitting of the displacement vs. time data via systems identification provides a transfer function. The transfer function may be used to calculate viscoelastic parameters.

Table 2: Comparison of output results in prediction of Q , shear moduli and relaxation time, for numerical simulation (ABAQUS) and new analytical model, using either logarithmic decrement or system identification.

	Analytic Method	Q		G_0 (Pa)	G_∞ (Pa)	τ (s)
Inputted or Predicted		2.53		10000	5000	0.05
ABAQUS simulation	Log. Dec.	2.93				
	Sys. ID	2.81		10950	4231	0.077
Analytical Model	Log. Dec.	2.50				
	Sys. ID	2.51		9954	4919	0.052

4.4.8 Effect of geometry and mass of the impactor on the outcome variables

It is clear that Q and therefore K are dependent on the pendulum-indenter-impact material system, as can be seen by **Equations 4.23 and 4.24**. Thus, Q and K will be functions of not only the impacted material, but also indenter geometry, mass of the pendulum, pendulum damping, etc. While the derived impact indentation equations (**Equations 4.23 and 4.24**) do not have explicit solutions for Q in terms of the mass and geometry (i.e., radius) of the probe, we can understand the trends by looking at the simple mass-spring-dashpot system. From **Equations 4.4 and 4.6** we see that Q scales with the square root of the mass and the square root of the material stiffness. These trends are mimicked in the more complete model, but must be solved numerically.

4.4.9 A complete mathematical model for impact indentation experiments

While **Section 4.4.3** provides a starting point for the analysis, to more accurately mimic the experimental setup we must include the effects of pendulum gravity and pendulum damping. We begin with a free body diagram (**Figure 4.1**). We assume that, since the angular displacements are small, the movement of the pendulum is only in the x direction, and thus the pendulum acceleration is linear rather than angular, and the inertia of the pendulum/indenter is represented by mass instead of moment of inertia. Therefore, the inertia of the indenter and the material response of the viscoelastic material are as described in **Equations 4.23 and 4.24**. The gravity term is:

$$F_g(\theta(t)) = mgL(\sin\theta_{eq} - \sin\theta(t)) \quad (4.36)$$

$$\approx F_g(u(t)) = mgL^*u(t)$$

where L^* is the ratio of the pivot-center of mass distance to the pivot-indenter distance. The pendulum has a damping force is:

$$F_d(t) = b(t) \frac{du}{dt}$$

Performing a force balance, and including an external load $F_{ext}(t)$:

$$F_{ext}(t) = m \frac{d^2u(t)}{dt^2} + b \frac{du(t)}{dt} + \frac{4R}{(1-\nu)} \int_0^t G(t-\tau) \frac{du(\tau)}{d\tau} d\tau + mgL^*u(t) \quad (4.37)$$

(Flat punch)

$$F_{ext}(t) = m \frac{d^2u(t)}{dt^2} + b \frac{du(t)}{dt} + \frac{8R^{1/2}}{3(1-\nu)} \int_0^t G(t-t') d(u^{3/2}(t')) + mgL^*u(t) \quad (4.38)$$

(Spherical impactor)

For the flat punch geometry, the same method may be used as in **Section 4.4.4** to predict the impact response from the characteristic polynomial:

$$\bar{P}(s) = ms^2 + bs + \frac{4R}{(1-\nu)} \left(G_\infty + \sum_{i=1}^n \frac{G_i s}{s + 1/\tau_i} \right) + mgL^* \quad (4.39)$$

and similar formulations may be used to extract the moduli and time constants from the impact indentation response, assuming the damping coefficient, gravity term, and external loads. Confirming these results with simulation and with experimental data should be pursued in future work.

4.5 Discussion

Applying this new model of impact indentation yields several insights as to how the system is expected to behave. This analytical approach also provides a new platform for predicting impact indentation results and analyzing experimental data.

The previously published model, while based on the same engineering principles as the current one, was oversimplified and therefore prone to misleading interpretation of results on highly compliant materials. Namely, the model did not take into account the coupling of velocity and external load on the pendulum. Simulations allowed for the decoupling of velocity and external load, and showed that the trends of K , Q and x_{max} with impact velocity were strongly affected by external load. In fact, these simulated data showed that K and Q are constant with impact velocity for linearly viscoelastic materials. The change with impact velocity is an artifact of the analytic procedure. For example, in the previous calculation of K , the conservation of energy did not include the external load term, which adds energy into the system during the experiment. Therefore, since K is normalized only to the kinetic energy into the system, the increase in K with impact velocity is an artifact of the coupled external load.

Theory suggests that K and Q are properties of the system (but not material properties) and are independent of the external force if delta or step inputs are applied. In fact they are both related to the poles of the mass-spring-dashpot system. Interestingly, it is readily shown that K and Q are essentially measurements of the same property in the case of a simple mass-spring-dashpot system; in other words, K is a function of only Q . However, it is important to note that this analysis neglects transients due to relaxation times from the generalized Maxwell model. Future work should determine the exact relationship between K and Q when using more complex material models.

While nonlinear mechanical properties are not included, it is of interest to understand the effect of nonlinear strain stiffening on Q and K . Simple investigation of a spring-mass-dashpot model suggests that increased strain stiffening is analogous to increasing the spring stiffness k , which would be expected to increase Q (**Section 4.2.1**). Since tissues and polymers often display nonlinear elastic properties, it is reasonable to question whether and how our engineering approximation may affect accurate prediction and analysis of impact indentation experimental data. If most of the stress in the sample leads to deformations in the linear viscoelastic regime, this model may be useful in analyzing data. Future work can assess the usefulness of our linear model via finite element simulations of linear viscoelastic vs. nonlinear viscoelastic models.

Further, this analytical model provides a more efficient platform for predicting the response of the system: displacement vs. time solutions were solved numerically in much less time than a finite element model, and the analytical parameters K and Q were determined with simple algebraic expressions. The inputs to the finite element method and to the analytical model are essentially the same: physical and mechanical properties, geometry, loading and velocity conditions, masses, etc. However, the analytical model is limited as it may not be used to include effects of adhesion, nonlinear mechanical properties, and complicated geometries beyond a flat punch or sphere on a semi-infinite halfspace. We note that these simple algebraic solutions for K and Q are only available for the flat punch geometry. While we may solve for displacement vs. time of the spherical impactor numerically from the nonlinear **Equation 4.23**, the Laplace transform is invalid for nonlinear ODEs, and K and Q are more difficult to predict directly.

This analytical model provides several new methods for measuring Q , and thus K , that are increasingly accurate. Logarithmic decrement is particularly convenient, but is based on a simple mass-spring-dashpot model only, and provides only two poles. Systems identification

assumes a transfer function and fits the curve, and will thus output several poles, from which K and Q as well as the dynamic moduli and time constants may be assessed. We have validated this analysis (**Table 2**), but we note that there is some error (<20% for elastic modulus and time constant) for ABAQUS simulated data. The reason for this error is unclear, but it could be due to nonlinear strains or a beveled probe that are not taken account in the analytical model used to fit the data.

Overall, this study presents a new way of analyzing impact indentation data. The new model provides a more rigorous interpretation of the previous analysis of impact indentation. It allows for both prediction of the experimental data from mechanical properties (which was attained previously by finite element modeling) and also extraction of mechanical properties (such as viscoelastic moduli and relaxation time constants) from experimental data. Further, assumption of a simple mass-spring-dashpot model, the basis of the previous analysis, now allows for relation of the variables K , Q and x_{\max} to each other; interestingly, K and Q are direct functions of one another. Finally, this work provides two data fitting methods – logarithmic decrement and systems identification – for more accurate measurement of K and Q as well as measurement of viscoelastic moduli and time constants. Since this work relied on simplified simulated finite element output, future work is necessary to implement these analyses for experimental impact indentation data.

5 References

1. Johnson, C. L. *et al.* Local mechanical properties of white matter structures in the human brain. *Neuroimage* **79**, 145–152 (2013).
2. Murphy, M. C. *et al.* Decreased brain stiffness in Alzheimer’s disease determined by magnetic resonance elastography. *J. Magn. Reson. Imaging* **34**, 494–498 (2011).
3. Pogoda, K. *et al.* Compression stiffening of brain and its effect on mechanosensing by glioma cells. *New J. Phys.* **16**, 075002 (2014).
4. Schregel, K., Wuerfel, E., Garteiser, P., Gemeinhardt, I. & Prozorovski, T. Demyelination reduces brain parenchymal stiffness quantified in vivo by magnetic resonance elastography. *Proc. Natl. Acad. Sci. U. S. A.* **109**, 6650–6655 (2012).
5. Wuerfel, J. *et al.* MR-elastography reveals degradation of tissue integrity in multiple sclerosis. *Neuroimage* **49**, 2520–2525 (2010).
6. Kalcioğlu, Z. I. *et al.* Tunable mechanical behavior of synthetic organogels as biofidelic tissue simulants. *J. Biomech.* **46**, 1583–1591 (2013).
7. Prange, M. T. & Margulies, S. S. Regional, directional, and age-dependent properties of the brain undergoing large deformation. *J. Biomech. Eng.* **124**, 244–252 (2002).
8. Sack, I. *et al.* The impact of aging and gender on brain viscoelasticity. *Neuroimage* **46**, 652–657 (2009).
9. Chatelin, S., Constantinesco, A. & Willinger, R. Fifty years of brain tissue mechanical testing: From in vitro to in vivo investigations. *Biorheology* **47**, 255–276 (2010).
10. Hyder, A, Wunderlich C, Puvanavhandra, P, Gururak G, K. O. The impact of traumatic brain injuries: a global perspective. *NeuroRehabilitation* **22**, 341–53 (2007).
11. Faul M, Xu L, Wald MM, C. V. Traumatic brain injury in the United States: emergency department visits, hospitalizations, and deaths. *Centers Dis. Control Prev. Natl. Cent. Inj. Prev. Control* 891–904 (2010). doi:10.1016/B978-0-444-52910-7.00011-8
12. Roozenbeek, B., Maas, A. I. R. & Menon, D. K. FOCUS ON TRAUMATIC BRAIN INJURY Changing patterns in the epidemiology of traumatic brain injury. *Nat. Publ. Gr.* **9**, 231–236 (2013).
13. Young, P. G., Qidwai, S. M., Bagchi, A., Kota, N. & Cotton, R. T. Developing a finite element head model for impact simulation in Abaqus. 1–13
14. Goriely, A. *et al.* Mechanics of the brain: perspectives, challenges, and opportunities. *Biomech. Model. Mechanobiol.* **14**, 931–965 (2015).

15. Cloots, R. J. H., Van Dommelen, J. a W., Nyberg, T., Kleiven, S. & Geers, M. G. D. Micromechanics of diffuse axonal injury: Influence of axonal orientation and anisotropy. *Biomech. Model. Mechanobiol.* **10**, 413–422 (2011).
16. Miller, K. *et al.* Modelling brain deformations for computer-integrated neurosurgery. *Int. j. numer. method. biomed. eng.* **26**, 117–138 (2010).
17. Shen, F. *et al.* Modified Bilston nonlinear viscoelastic model for finite element head injury studies. *J. Biomech. Eng.* **128**, 797–801 (2006).
18. Hemphill, M. A., Dauth, S., Yu, C. J., Dabiri, B. E. & Parker, K. K. Traumatic brain injury and the neuronal microenvironment: A potential role for neuropathological mechanotransduction. *Neuron* **85**, 1177–1192 (2015).
19. Cloots, R. J. H., Van Dommelen, J. a W., Kleiven, S. & Geers, M. G. D. Multi-scale mechanics of traumatic brain injury: Predicting axonal strains from head loads. *Biomech. Model. Mechanobiol.* **12**, 137–150 (2013).
20. *Linking Helmet Protection to Brain Injury. In: Review of Department of Defense Test Protocols for Combat Helmets.* (The National Academies Press, 2014).
21. Miller, K. *Biomechanics of the Brain.* (Springer, 2011).
22. Prevost, T. P., Balakrishnan, A., Suresh, S. & Socrate, S. Biomechanics of brain tissue. *Acta Biomater.* **7**, 83–95 (2011).
23. Kalcioğlu, Z. I. *et al.* Dynamic impact indentation of hydrated biological tissues and tissue surrogate gels. *Philos. Mag.* **91**, 1339–1355 (2011).
24. Bhattacharjee, D., Kumar, A. & Biswas, I. Energy absorption and dynamic deformation of backing material for ballistic evaluation of body armour. *Def. Sci. J.* **63**, 462–466 (2013).
25. Canovic, E. P. *et al.* Characterizing Multi-scale Mechanical Properties of Brain Tissue Using Atomic Force Microscopy, Impact Indentation, and Rheometry. *J. Vis. Exp. Press* (2016).
26. Budday, S. *et al.* Mechanical properties of gray and white matter brain tissue by indentation. *J. Mech. Behav. Biomed. Mater.* **46**, 318–330 (2015).
27. Mrozek, R. a., Cole, P. J., Otim, K. J., Shull, K. R. & Lenhart, J. L. Influence of solvent size on the mechanical properties and rheology of polydimethylsiloxane-based polymeric gels. *Polymer (Guildf).* **52**, 3422–3430 (2011).
28. Qing, B. & Van Vliet, K. J. Hierarchical design of synthetic gel composites optimized to mimic the impact energy dissipation response of brain tissue. *Mol. Syst. Des. Eng.* (2016). doi:10.1039/C6ME00051G

29. Franceschini, G., Bigoni, D., Regitnig, P. & Holzapfel, G. A. Brain tissue deforms similarly to filled elastomers and follows consolidation theory. *J. Mech. Phys. Solids* **54**, 2592–2620 (2006).
30. Franze, K., Janmey, P. a & Guck, J. Mechanics in neuronal development and repair. *Annu. Rev. Biomed. Eng.* **15**, 227–51 (2013).
31. Brands, D. W. a., Peters, G. W. M. & Bovendeerd, P. H. M. Design and numerical implementation of a 3-D non-linear viscoelastic constitutive model for brain tissue during impact. *J. Biomech.* **37**, 127–134 (2004).
32. Van Dommelen, J. a W., Hrapko, M. & Peters, G. W. M. Mechanical Properties of Brain Tissue: Characterisation and Constitutive Modelling. *Mechanosensitivity Nerv. Syst.* 249–281 (2009). doi:10.1007/978-1-4020-8716-5_12
33. Hrapko, M., Dommelen, J. A. W. Van, Peters, G. W. M. & Wismans, J. S. H. M. The mechanical behaviour of brain tissue : Large strain response and constitutive modelling. **43**, 623–636 (2006).
34. Van Dommelen, J. a W., Hrapko, M. & Peters, G. W. M. *Mechanical properties of brain tissue: Characterisation and constitutive modelling. Mechanosensitivity of the Nervous System* (2009). doi:10.1007/978-1-4020-8716-5_12
35. Fung, Y. C. *Biomechanics: Mechanical Properties of Living Tissues*. (Springer-Verlag, 1988).
36. Lakes, R. *Viscoelastic Materials*. (Cambridge Univeristy Press, 2009).
37. Djordjević, V. D., Jarić, J., Fabry, B., Fredberg, J. J. & Stamenović, D. Fractional derivatives embody essential features of cell rheological behavior. *Ann. Biomed. Eng.* **31**, 692–699 (2003).
38. Arruda, E. M. & Boyce, M. C. A three-dimensional constitutive model for the large stretch behavior of rubber elastic materials. *J. Mech. Phys. Solids* **41**, 389–412 (1993).
39. Tyler, W. J. The mechanobiology of brain functio. *Nat. Rev. Neurosci.* **13**, 867–878 (2012).
40. Franceschini, G., Bigoni, D., Regitnig, P. & Holzapfel, G. a. Brain tissue deforms similarly to filled elastomers and follows consolidation theory. *J. Mech. Phys. Solids* **54**, 2592–2620 (2006).
41. Cheng, S. & Bilston, L. E. Unconfined compression of white matter. *J. Biomech.* **40**, 117–124 (2007).

42. Lynne Bilston, Zizhen Liu, N. P.-T. Linear Viscoelastic Properties of Bovine Brain Tissue in Shear. *Biorheology* **34**, 377–385 (1997).
43. Brands, D. W. A., Bovendeerd, P. H. M., Peters, G. W. N. & Bree, J. L. M. J. Van. Comparison of the Dynamic Behaviour of Brain Tissue and Two Model Materials. (1999).
44. Kruse, S. a. *et al.* Magnetic resonance elastography of the brain. *Neuroimage* **39**, 231–237 (2008).
45. Elkin, B. S., Azeloglu, E. U., Costa, K. D. & Morrison, B. Mechanical heterogeneity of the rat hippocampus measured by atomic force microscope indentation. *J. Neurotrauma* **24**, 812–822 (2007).
46. Lu, Y. *et al.* Viscoelastic properties of individual glial cells and neurons in the CNS. **103**, 17759–17764 (2006).
47. McGarry, M. D. J. *et al.* Suitability of poroelastic and viscoelastic mechanical models for high and low frequency MR elastography. *Med. Phys.* **42**, 947–957 (2015).
48. Howard, J. *Mechanics of Motor Proteins and the Cytoskeleton*. (Sinauer Associates, 2001).
49. Lau, L. W., Cua, R., Keough, M. B., Haylock-Jacobs, S. & Yong, V. W. Pathophysiology of the brain extracellular matrix: a new target for remyelination. *Nat. Rev. Neurosci.* **14**, 722–9 (2013).
50. Janmey, P. a, Georges, P. C. & Hvidt, S. Basic rheology for biologists. *Methods Cell Biol.* **83**, 3–27 (2007).
51. Curatolo, P., Bombardieri, R. & Jozwiak, S. Tuberous sclerosis. *Lancet* **372**, 657–668 (2008).
52. Meikle, L. *et al.* A mouse model of tuberous sclerosis: neuronal loss of Tsc1 causes dysplastic and ectopic neurons, reduced myelination, seizure activity, and limited survival. *J. Neurosci.* **27**, 5546–58 (2007).
53. Lewis, W. W. *et al.* Impaired language pathways in tuberous sclerosis complex patients with autism spectrum disorders. *Cereb. Cortex* **23**, 1526–1532 (2013).
54. Canovic, E. P. *et al.* Probing mechanical properties of brain in a tuberous sclerosis model of autism. *Prep.* (2016).
55. Cui, J., Lee, C. H., Delbos, A., McManus, J. J. & Crosby, A. J. Cavitation rheology of the eye lens. *Soft Matter* **7**, 7827 (2011).

56. Jansen, L. E., Birch, N. P., Schiffman, J. D., Crosby, A. J. & Peyton, S. R. Mechanics of intact bone marrow. *J. Mech. Behav. Biomed. Mater.* **50**, 299–307 (2015).
57. Zimmerlin, J. a., McManus, J. J. & Crosby, A. J. Cavitation rheology of the vitreous: mechanical properties of biological tissue. *Soft Matter* **6**, 3632 (2010).
58. Pavlovsky, L., Ganesan, M., Younger, J. G. & Solomon, M. J. Elasticity of microscale volumes of viscoelastic soft matter by cavitation rheometry. *Appl. Phys. Lett.* **105**, 114105 (2014).
59. Zimmerlin, J. a., Sanabria-DeLong, N., Tew, G. N. & Crosby, A. J. Cavitation rheology for soft materials. *Soft Matter* **3**, 763 (2007).
60. Kundu, S. & Crosby, A. J. Cavitation and fracture behavior of polyacrylamide hydrogels. *Soft Matter* **5**, 3963 (2009).
61. Cui, J., Lee, C. H., Delbos, A., McManus, J. J. & Crosby, A. J. Cavitation rheology of the eye lens. *Soft Matter* **7**, 7827 (2011).
62. Chin, M. S. *et al.* Cavitation rheology as a potential method for in vivo assessment of skin biomechanics. *Plast. Reconstr. Surg.* **131**, 303e–305e (2013).
63. Hutchens, S. B. & Crosby, A. J. Soft-solid deformation mechanics at the tip of an embedded needle. *Soft Matter* **10**, 3679–84 (2014).
64. Delbos, A., Cui, J., Fakhouri, S. & Crosby, A. J. Cavity growth in a triblock copolymer polymer gel. *Soft Matter* **8**, 8204 (2012).
65. Tongue, B. H. *Principles of Vibration*. (Oxford University Press, Inc., 1996).
66. Adityan, A. K. Computational Design of Viscoelastic Gels with Tunable Mechanical Energy Dissipation. (2014).
67. Calvit, H. H. Numerical Solution of the Problem of Impact of a Rigid Sphere onto a Linear Viscoelastic Half-Space and Comparison with Experiment. *Int. J. Solids Struct.* **3**, 951–966 (1967).
68. Chen, C. P. & Lakes, R. S. Design of viscoelastic impact absorbers: Optimal material properties. *Int. J. Solids Struct.* **26**, 1313–1328 (1990).
69. Johnson, K. L. *Contact Mechanics*. (Cambridge Univeristy Press, 1985).
70. Cheng, L., Xia, X., Yu, W., Scriven, L. E. & Gerberich, W. W. Flat-Punch Indentation of Viscoelastic Material. **38**, 10–22 (2000).

6 Appendix

Logarithmic decrement may be used to measure Q or ζ from peaks of a damped oscillation and frequency. Here we demonstrate that this works for the impact indentation displacement vs. time response, provided that the material model is a spring-mass-dashpot, and that the force input is an inertial load with a superimposed constant load. The solution for velocity over time will be:

$$u(t) = C_1 e^{-\zeta \omega_n t} \sin(\omega_n \sqrt{1 - \zeta^2} t) + C_2 - C_2 e^{-\zeta \omega_n t} \cos(\omega_n \sqrt{1 - \zeta^2} t)$$

This may be written in terms of complex exponentials as

$$u(t) = C_3 e^{-\zeta \omega_n t} e^{i \omega_n \sqrt{1 - \zeta^2} t - \delta} + C_2$$

where δ is the resulting phase lag from combining the sine and cosine terms. If we use a modified logarithmic decrement formula, and assuming $\sqrt{1 - \zeta^2} \approx 1$ we get:

$$\begin{aligned} \Delta &= \frac{1}{n} \ln \frac{x(t) - x(t + \frac{1}{2}nT)}{x(t + nT) - x(t + \frac{3}{2}nT)} \\ &= \frac{1}{n} \ln \frac{(C_3 e^{-\zeta \omega_n t} e^{i \omega_n t - \delta} + C_2) - (C_3 e^{-\zeta \omega_n (t + \frac{1}{2}nT)} e^{i \omega_n (t + \frac{1}{2}nT) - \delta} + C_2)}{(C_3 e^{-\zeta \omega_n (t + nT)} e^{i \omega_n (t + nT) - \delta} + C_2) - (C_3 e^{-\zeta \omega_n (t + \frac{3}{2}nT)} e^{i \omega_n (t + \frac{3}{2}nT) - \delta} + C_2)} \end{aligned}$$

C_2 and δ cancel:

$$= \frac{1}{n} \ln \frac{(C_3 e^{-\zeta \omega_n t} e^{i \omega_n t}) - (C_3 e^{-\zeta \omega_n (t + \frac{1}{2}nT)} e^{i \omega_n (t + \frac{1}{2}nT)})}{e^{-\zeta \omega_n nT} e^{i \omega_n nT} [(C_3 e^{-\zeta \omega_n (t)} e^{i \omega_n (t)}) - (C_3 e^{-\zeta \omega_n (t + \frac{1}{2}nT)} e^{i \omega_n (t + \frac{1}{2}nT)})]}$$

Since $e^{i \omega_n nT} = 1$,

$$\Delta = \frac{1}{n} \ln(e^{\zeta \omega_n nT}) = \zeta \omega_n T$$

$$\Delta = 2\pi\zeta$$